Molecule Detection by Sum Frequency Mixing of Mid-Infrared Laser Pulses

Moleküldetektion durch Summenfrequenzmischung mittelinfraroter Laserpulse
Dissertation von Benedikt Burger, Oktober 2024

TECHNISCHE
UNIVERSITÄT
DARMSTADT

Fachbereich Physik
Institut für Angewandte Physik
Nichtlineare Optik / Quantenoptik

Molecule Detection by Sum Frequency Mixing of Mid-Infrared Laser Pulses

Vom Fachbereich Physik
der Technischen Universität Darmstadt

zur Erlangung des Grades
eines Doktors der Naturwissenschaften
(Dr. rer. nat.)

genehmigte Dissertation von
M.Sc. Benedikt Burger

Referent: Prof. Dr. Thomas Halfmann
Korreferent: Prof. Dr. Vincent Bagnoud

Tag der Einreichung: 15. Oktober 2024
Tag der Prüfung: 11. November 2024

Darmstadt 2024
D17

Benedikt Burger: Molecule Detection by Sum Frequency Mixing of Mid-Infrared Laser Pulses
Darmstadt, Technische Universität Darmstadt
Jahr der Veröffentlichung der Dissertation auf TUprints: 2024
URN: urn:nbn:de:tuda-tuprints-283092

Tag der mündlichen Prüfung: 11.11.2024

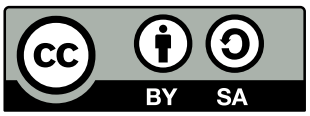

Contents

Abbreviations

APD avalanche photodiode.

AR anti-reflective.

BBO beta-barium borate.

CARS coherent anti-Stokes Raman spectroscopy.

CO_2 carbon dioxide.

CW continuous-wave.

DFM difference frequency mixing.

FWHM full width at half maximum.

FWM four wave mixing.

HCl hydrogen chloride.

HR highly reflective.

HT highly transmissive.

HWHM half width at half maximum.

JSON JavaScript Object Notation.

LNB lithum niobate.

N_2 nitrogen.

NLO nonlinear optics.

OPA optical parametric amplifier.

OPO optical parametric oscillator.

PMT photomultiplier tube.

PPLN periodically poled lithium niobate.

PyPI Python Package Index.

RPC remote procedure call.

SFM sum frequency mixing.

SHG second harmonic generation.

SNR signal-to-noise ratio.

TCP transmission control protocol.

THG third harmonic generation.

UV ultraviolet.

Introduction

There are many spectroscopic techniques available for detecting molecular species, each with its own advantages and limitations. Some methods, such as absorption spectroscopy or fluorescence, rely on the linear interaction of light with matter. While effective in many applications, these linear techniques often suffer from limited sensitivity and selectivity, particularly when dealing with complex mixtures or low-concentration samples.

In contrast, nonlinear optical (NLO) spectroscopy offers significant advantages in molecular detection by exploiting higher-order interactions between light and matter [1]. These techniques generate highly directional, coherent signals with a frequency different from the probing frequency, which allows effective filtering and results in an excellent signal-to-noise ratio (SNR). They can also, like linear methods, achieve species-selectivity, especially when the nonlinear optics (NLO) response is resonantly enhanced. As molecular energy levels, especially of molecular rovibrational states, are characteristic for a gas species, they permit to identify the gas species at hand of its resonance lines in a spectrum, similar to a fingerprint [2, 3]. This sensitivity make NLO methods particularly valuable for applications where traditional linear techniques fall short [4].

There are several techniques which exploit resonance enhancement in order to detect molecular gas species. In the following description, we use $|\mathrm{e}\rangle$ to denote the first excited electronic state and $|v = i\rangle$ for the vibrational state of the electronic ground state with vibrational quantum number i. The current work horse in gas spectrometry is coherent anti-Stokes Raman spectroscopy (CARS), a resonantly enhanced four wave mixing (FWM) process [5–7]. Fig. 1 (a) shows with an exemplary molecular level scheme, how a pump wave ω_p and a Stokes wave ω_St generate an anti-Stokes wave at the signal frequency $\omega_\mathrm{s} = \omega_\mathrm{p} - \omega_\mathrm{St} + \omega_\mathrm{p}$ via a four wave difference frequency mixing (DFM) process. It probes the two-photon transition at $\omega_\mathrm{t} = \omega_\mathrm{p} - \omega_\mathrm{St}$ exploiting resonance enhancement.

Typically, the interacting waves are in the visible or ultraviolet (UV) range [2], while the probed rovibrational transition is in the mid-infrared. Therefore, also the measured anti-Stokes signal is in the visible or UV regime, where sensitive detectors are available. The single-photon transition dipole moment between the ground state and electronically excited state is typically a few $10^{-30}\,\mathrm{C\,m}$.

However, CARS requires typically two high-power narrowband lasers with a finely tuned frequency difference. Ultra-broadband lasers (with a bandwidth around 100 THz) can produce the pump and Stokes radiation at the same time, but introduce additional challenges regarding frequency sensitivity and off-resonant background [3]. Additionally, in a typical molecule, the one- and three-photon detunings to the excited electronic state are quite large with several 100 THz, reducing the nonlinear susceptibility and thus the effectiveness of this method.

Third harmonic generation (THG) in the mid-infrared among vibrational states is a simpler approach with a single fundamental wave ω_f, which generates a signal at $\omega_\mathrm{THG} = 3\omega_\mathrm{f}$. It not only exploits resonance enhancement with one-, two-, or three-photon transitions, as Fig. 1 (b) shows, but also profits from small detunings (a

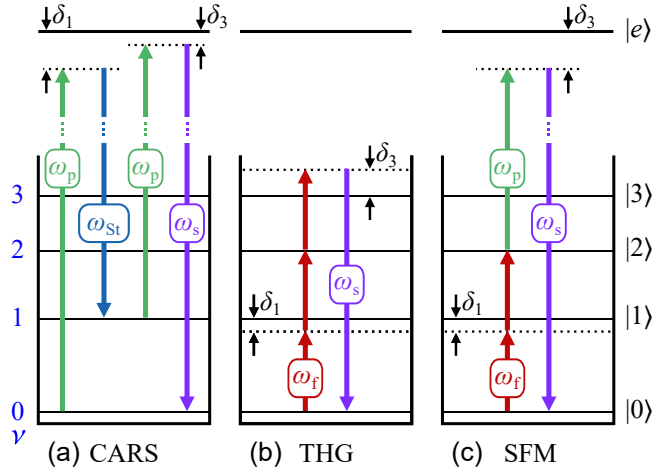

Figure 1: Coupling schemes for (a) coherent anti-Stokes Raman spectroscopy (CARS), (b) third harmonic generation (THG), and (c) sum frequency mixing (SFM). For simplicity, we show only the vibrational states $|\nu\rangle$ of the electronic ground state, but not their rotational sub structure, nor details of the excited electronic state(s) $|e\rangle$. Arrows indicate laser fields at the fundamental (ω_f, red), probe (ω_p, green, in the case of CARS also called pump), Stokes (ω_{St}, blue), and generated signal (ω_s, purple, in the case of CARS also called anti-Stokes) frequency while δ_i indicates the i-photon detuning. We assume the lasers are tuned to two-photon resonance with vibrational states in the electronic ground state, providing an example of resonance enhancement without the absorption typically associated with single-photon resonance.

few hundred GHz) as all three transitions can be close to resonance simultaneously. However, the rovibrational transition dipole moments are typically only less than $10^{-30}\,\mathrm{C\,m}$, and for the overtone transition from the state $|\nu = 3\rangle$ to the ground state $|\nu = 0\rangle$, it is even less, around $0.001 \times 10^{-30}\,\mathrm{C\,m}$. Nevertheless, the smaller detunings outweigh these low transition dipole moments yielding a larger nonlinear susceptibility than CARS for a typical molecule.

Furthermore, the fundamental wave, close to rovibrational transitions, is in the mid-infrared regime, thus, also the third harmonic is in the mid-infrared regime. This requires a high-power mid-infrared light source with a narrow spectral bandwidth ($< 1\,\mathrm{GHz}$) in order to resolve closely spaced resonances. It also requires a suitable detector for the mid-infrared THG signal. Photomultiplier tubes (PMTs) are not suitable in the mid-infrared regime as their photocathodes are not sensitive for such long wavelengths. Avalanche photodiodes (APDs) are an appropriate choice in that case. However, they have a substantially lower internal gain of 10–100 compared to the gain of a PMT with 10^5–10^6 or beyond. Moreover, the aperture of an APD is typically much smaller (diameters far below 1 mm) than the active area of the photo-cathode in a PMT (diameters of 1 cm or more). This makes alignment and applications with APD detection under realistic conditions, e.g, for environmental sensing, more difficult. Finally, PMTs are usually cheaper compared to an APD, which may even require an additional electric amplifier at the output. Hence, it would be preferable to apply a PMT to monitor also long-wavelength signals.

Previously, our group implemented THG to detect hydrogen chloride (HCl) down to a pressure of 1 mbar [8]. In this work, we explore related alternatives to this approach, which permit more sensitive molecular detection. Our focus is particularly

on techniques that shift the signal to the visible spectral range, allowing us to utilize detectors with higher sensitivity, like PMTs.

Up-converting a coherent mid-infrared signal to a more accessible frequency range, such as the visible spectrum, is a well-established technique in NLO [9–11]. This process typically involves sum frequency mixing (SFM) of a weak mid-infrared signal with a strong pump laser in the near-infrared or visible range, using a conventional nonlinear optical crystal. The pump beam is often readily available as residual fixed-frequency radiation from the laser system that provides the fundamental radiation for the experiment. Due to the high nonlinearity of appropriate crystals, the conversion efficiency (defined as the ratio of generated visible photons vs. incoming mid-infrared photons) can approach unity with a sufficiently strong pump wave [12].

Instead of up-converting the THG signal, we can directly generate visible or near-infrared radiation within the medium itself while maintaining the small detunings characteristic of THG. This is achieved through SFM, where two mid-infrared fundamental photons, tuned close to rovibrational resonances (as in resonantly enhanced THG), are combined with a probe photon of another frequency ω_p. Typically, the laser system contains more than enough pulse energy at a fixed frequency, which can serve as the probe pulse. If the probe photon has a higher energy, the signal frequency can be visible or near-infrared which allows to use other detectors with possibly better characteristics. This higher energy also allows to use the excited electronic state $|\mathrm{e}\rangle$ with a higher transition dipole moment of typically a few $10^{-30}\,\mathrm{C\,m}$, instead of the vibrational state $|v=3\rangle$ (see Fig. 1 (c)). At the same time, the single-photon detuning δ_1 remains as small as in the case of THG. Pellin and Yardley suggested this method already in 1976 [13], but experimental studies have been scarce since [14].

This work is structured into four chapters. In the first chapter, we introduce and compare the principles of THG spectroscopy and SFM in the medium. The second chapter presents the test gas HCl along with the laser system generating the fundamental radiation. In the third chapter, we provide an experimental comparison between these two spectroscopic methods. This includes numerical simulations of THG and SFM in HCl, followed by a detailed experimental analysis of their spectra, SNR, input and pressure dependences, as well as their detection limits. The fourth chapter focuses on comparing the direct detection of the THG signal to its up-converted detection. It covers preliminary tests, the experimental setup, and the results of this comparison.

Chapter 1

Resonantly Enhanced THG and SFM Spectroscopy

In this chapter we introduce the nonlinear processes of resonantly enhanced THG and SFM, we show their dependence on resonances, and how it can be applied to species detection. Textbooks [15] and review articles [9, 16] offer a more in depth description of these processes. Finally, we compare both methods.

1.1 Resonantly Enhanced THG Spectroscopy

THG is a third order effect of nonlinear optics. Therefore, it exists also in isotropic media like gases, unlike second order effects. Similar to second order nonlinear optics, there are several different processes how the participating waves interact in third order nonlinear optics. They all have in common that the nonlinear dielectric polarization is proportional to the product of the electric field strengths E_1, E_2, and E_3 of the incoming waves and proportional to the nonlinear dielectric susceptibility of third order $\chi^{(3)}$, which depends on the actual process and frequencies. A typical measurement value is the power of an electromagnetic wave and not the electric field nor the dielectric polarization. As the power depends quadratically on both of latter quantities, the power of the FWM wave is $P_{\mathrm{FWM}} \propto |\chi^{(3)}|^2\, P_1 \cdot P_2 \cdot P_3$ with the power of the incoming waves P_i. Let ω_1, ω_2, and ω_3 be the frequencies of incoming waves, then they can combine to the sum frequency $\omega_{\mathrm{SFM}} = \omega_1 + \omega_2 + \omega_3$ or they can combine to a difference frequency $\omega_{\mathrm{DFM1}} = \omega_1 + \omega_2 - \omega_3$ or $\omega_{\mathrm{DFM2}} = \omega_1 - \omega_2 - \omega_3$. Any permutation of the frequencies is possible as long as the resulting frequency remains positive.

THG is a special case of SFM, where all three input frequencies are equal. In this case, the resulting frequency is $\omega_{\mathrm{THG}} = 3\omega_{\mathrm{f}}$ with the fundamental frequency ω_{f}. For a fundamental beam with a Gaussian spatial beam profile and the power P_{f}, the resulting signal power P_{THG} is [15]

$$P_{\mathrm{THG}}(\omega_{\mathrm{THG}};\, \omega_{\mathrm{f}}) = \frac{\omega_{\mathrm{THG}}\, \omega_{\mathrm{f}}^3}{4\pi^2 \epsilon_0^2 c^6}\; b^{-2}\, |\, \chi^{(3)}|^2\, |J_3(\Delta k)|^2\, P_{\mathrm{f}}^3, \tag{1.1}$$

with the vacuum permittivity ϵ_0 and the speed of light c. The confocal parameter b and the phase-matching integral J_3 take into account beam focusing and phase evolution in the medium. See Ref. [8] for a more thorough introduction.

The first material property in Eq. 1.1 is the nonlinear dielectric susceptibility. For

the states $|i\rangle$ of a material it is [15] [1]

$$\chi^{(3)}(\omega_{\mathrm{THG}};\omega_{\mathrm{f}}) = \frac{1}{\epsilon_0\hbar^3}\sum_t \frac{\rho\,\mu_{10}\,\mu_{21}\,\mu_{32}\,\mu_{30}}{(\delta_1-\mathrm{i}\gamma_1)(\delta_2-\mathrm{i}\gamma_2)(\delta_3-\mathrm{i}\gamma_3)}, \tag{1.2}$$

with the number density ρ of molecules in the ground state $|0\rangle$, the single-photon detuning $\delta_1 = \omega_{01}-\omega_{\mathrm{f}}$, the two-photon detuning $\delta_2 = \omega_{02}-2\omega_{\mathrm{f}}$, the three-photon detuning $\delta_3 = \omega_{03}-3\omega_{\mathrm{f}}$, involving transition frequencies ω_{ij} between states $|i\rangle$ and $|j\rangle$, the corresponding transition dipole moments μ_{ij}, and the dephasing rates (linewidth) γ_i. The summation is over all transition paths t, that is over all sets of any three states. It is apparent, that a single summation term becomes large, whenever one or several of the detunings δ_i are small compared to the linewidth, which is at or near resonance. This effect is called resonance enhancement leading to the name *resonantly enhanced third harmonic generation*.

Also the phase-matching integral in Eq. 1.1 depends on the material as it is [15]

$$J_3(\Delta k) = \int_{z_0}^{z_1} \frac{e^{\mathrm{i}\,\Delta k z}\mathrm{d}z}{(1+2\mathrm{i}z/b)^2}, \tag{1.3}$$

for collinearly propagating Gaussian beams, with focus at $z=0$, interaction region between z_0 and z_1, and the wave vector mismatch $\Delta k = 3k_{\mathrm{f}} - k_{\mathrm{THG}}$ involving the wave vectors $k_i = n_i\omega_i/c$ with the refractive indices n_i, which contain the absorption in the imaginary part. Note that there is no standard convention for the sign of the wave vector mismatch; we follow the definition provided by Boyd [15]. Its wavelength dependence is small compared to the nonlinear dielectric susceptibility, with dispersion being the primary factor driving this dependence.

Typically, the refractive index is directly proportional to the pressure, meaning the wave vector mismatch also varies with pressure, thus altering the phase-matching integral across different pressures. Fig. 1.1 shows a numerical solution for the phase-matching as a function of wave vector mismatch for various confocal parameters. As the THG power is inversely proportional to the square of the confocal parameter, we include it in this figure.

Regardless of the confocal parameter, the phase-matching integral shows a maximum for positive wave vector mismatch, accompanied by smaller side peaks. As the confocal parameter increases, the location of the peak shifts closer to zero wave vector mismatch, while the maximum value of the integral also decreases. For the limit of infinite confocal parameter, that is plain waves, and for a finite interaction length, Eq. 1.3 results analytically in a sinc function, explaining the side peaks.

The nonlinear methods investigated in this work aim to identify molecular species. A typical molecule exhibits one or more vibrational modes with nearly uniformly distributed states and a transition dipole moment of approximately $\mu = 1\times10^{-30}\,\mathrm{C\,m}$. The vibrational transition frequencies are typically in the mid-infrared regime. Due to the small anharmonicity usually present in these modes, overtone transitions with

[1] The equation contains more terms, which represent SFM starting from an excited state or represent DFM. We do not show these terms as we consider THG and molecules in their vibronic ground state due to a thermal population distribution. We also neglect the tensor character of the transition dipole moments and of the dielectric susceptibility as it does not alter the results of our discussion.

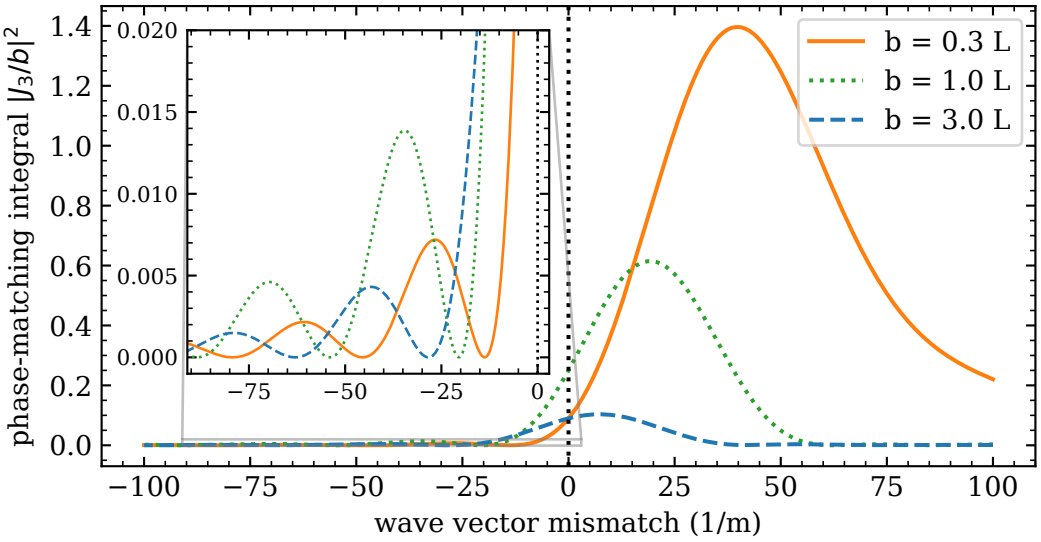

Figure 1.1: Absolute square value of the phase-matching integral divided by the confocal parameter vs. wave vector mismatch for different confocal parameters in unit of interaction length $L = z_1 - z_0$. The orange line gives an example for tight focusing, $b = 0.3L$, the dotted green line for confocal focusing, $b = L$, and the dashed blue line for loose focusing, $b = 3L$. We assume the focus to be in the center of the interaction region, $z_1 = -z_0$. The inset zooms in on the negative part of the wave vector mismatch axis.

$|\Delta v| > 1$ are possible, although the associated transition dipole moments are much smaller, typically around $\mu_{30} = 0.001 \times 10^{-30}$ C m for the third overtone, where v denotes the vibrational quantum number. Additionally, molecules can rotate along one or more axes, with transition frequencies that are typically much smaller than vibrational ones. As a result, rotational states, with the rotational quantum number N, can be considered substates of the vibrational states. The combined vibrational and rotational states are unique to each molecular species.

The power of the THG signal depends on the fundamental frequency, as well as the distribution of vibrational and rotational states and their respective transition dipole moments. Consequently, the THG spectrum itself is characteristic of a particular molecular species. The fundamental wave can exhibit one-, two-, or three-photon resonances. Typically, THG drives vibrational transitions with $\Delta v = 1$ which have almost equal transition frequencies, see Fig. 1. Therefore, the non-resonant detunings are usually around 1 THz. However, double or triple resonances are rare due to the small anharmonicity of typical vibrational modes and the complexity of the rotational substructure.

While one-photon resonances lead to resonance enhancement, they are also accompanied by strong absorption of the fundamental wave. For three-photon resonances, the THG signal also experiences absorption, but since the overtone transition is typically very weak (several orders of magnitude smaller in transition dipole moment) this effect is usually negligible.

To resolve different resonances, the fundamental wave must be spectrally narrowband, ideally less than 1 GHz for small molecules, and even narrower for larger molecules. Additionally, the fundamental power needs to be high due to the small

overtone transition dipole moment μ_{30} and the low particle density of gases at low pressure. This often necessitates the use of laser pulses with durations in the nanosecond range.

1.2 Resonantly Enhanced SFM Spectroscopy

THG represents the simplest form of third order SFM processes, relying on a single input frequency. Introducing additional input frequencies beyond those used in THG enables tuning of the output frequency while maintaining resonance enhancement. For instance, two mid-infrared photons can be two-photon resonant and have a small single-photon detuning, similar to THG, while a third photon in the near-infrared shifts the output frequency to the near-infrared or even visible range. Moreover, SFM allows for better optimization of the participating frequencies to match the specific molecular transitions, which can increase the nonlinear susceptibility by accessing transitions with larger dipole moments or lower detunings.

The power of the SFM wave is a more general form of Eq. 1.1 with the input frequencies ω_1, ω_2, and ω_3. The resulting power is

$$P(\omega_{\mathrm{SFM}};\, \omega_1, \omega_2, \omega_3) = \frac{\omega_{\mathrm{SFM}}\, \omega_1\, \omega_2\, \omega_3}{4\pi^2 \epsilon_0^2 c^6}\; b^{-2}\, |\, \chi^{(3)}|^2\, |J_3(\Delta k)|^2\, P_1\, P_2\, P_3, \tag{1.4}$$

with the powers P_i of the corresponding waves ω_i instead of the fundamental power P_f. In the nonlinear susceptibility $\chi^{(3)}$ (Eq. 1.2) a transition path t is a set of any three states and any permutation of the input frequencies. Therefore, the one-photon detuning is $\delta_1 = \omega_{01} - \omega_a$, the two-photon detuning $\delta_2 = \omega_{02} - \omega_a - \omega_b$, and the three-photon detuning $\delta_3 = \omega_{03} - \omega_a - \omega_b - \omega_c$ with a, b, and c being any permutation of 1, 2, and 3. The wave vector mismatch in the phase-matching integral J_3 (Eq. 1.3) is now $\Delta k = k_1 + k_2 + k_3 - k_{\mathrm{SFM}}$ involving the wave vectors $k_i = n_i \omega_i / c$ with the refractive indices n_i.

1.3 Comparison of THG and SFM Spectroscopy

To compare the expected nonlinear dielectric susceptibility for resonantly enhanced THG and SFM using Eq. 1.2, we assume typical values for a small molecule: a transition frequency of 1 000 THz and a transition dipole moment of 3×10^{-30} C m for electronic transitions. The transition dipole moment between neighboring vibrational states of the same electronic state ($\Delta v = \pm 1$) is 1×10^{-30} C m, and it is 0.001×10^{-30} C m for the third vibronic overtone transition. The Doppler broadened linewidth is assumed to be 1 GHz (full width at half maximum (FWHM)) and the pressure is 1 mbar with all molecules considered to be in the state $|v = 0\rangle$. At such a low pressure, pressure broadening is negligible, as we will discuss later.

For resonantly enhanced THG in a typical molecule with a single resonance ($\delta_i = 0$) and off-resonant detunings of δ_j, $\delta_k = 1$ THz, the expected absolute value for $\chi^{(3)}$ is approximately $100\,\mathrm{pm^2/V^2}$. To improve these results, focusing on enhancing the overtone transition dipole moment appears promising.

By employing SFM with two mid-infrared fundamental photons and a near-infrared or visible probe photon, the probe photon does not couple to the state $|v = 3\rangle$

of the electronic ground state, but rather to an excited electronic state. This allows the product of the relevant transition dipole moments (μ_{32}, μ_{30}) to increase by several orders of magnitude. Despite the large detuning to the excited electronic state (1 000 THz), this increase compensates for the detuning, resulting in a nonlinear dielectric susceptibility of approximately 1 000 $\mathrm{pm}^2/\mathrm{V}^2$, which is an order of magnitude larger than that achieved with THG.

The signal power is not only dependent on the nonlinear susceptibility but is also proportional to the input wave powers and their frequencies. Therefore, a higher probe frequency can enhance the generated power. More importantly, there is often residual fixed-frequency pulse energy available from the laser system that generates the fundamental radiation. This fixed-frequency radiation can serve as the probe wave, potentially providing more pulse energy than the fundamental wave itself has.

Chapter 2

Experimental Setup

In order to experimentally compare THG with its alternative SFM, we need an actual molecule, a light source with the appropriate wavelength and pulse energy, and a suitable detection setup.

In this chapter we describe the relevant properties of our test gas and show the different parts of our laser system, which generates the fundamental radiation for THG in this test gas. We published a description of the laser system and its characteristics in "Applied Physics B" [17]. For details on the control software framework we developed to manage the entire experimental setup, refer to Appendix B.

2.1 Test Gas Hydrogen Chloride

As a test gas, the molecule should be available and stable for ease of use. Furthermore, we need to generate the necessary fundamental radiation and effectively detect the resulting signal wave. Generally, even small molecules with large vibrational quanta have vibrational transition wavelengths in the range of several micrometers. In contrast, larger molecules with smaller vibrational quanta have longer transition wavelengths, which can complicate the process of light generation and detection. Lastly, the molecule should be scientifically relevant.

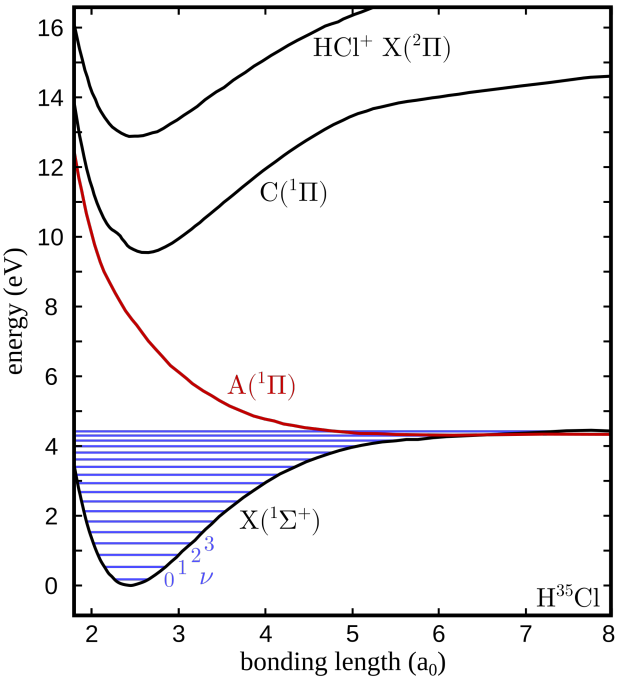

Figure 2.1: Potential energy of the first three electronic states $X(^1\Sigma^+)$, $A(^1\Pi)$, and $C(^1\Pi)$, and of the ionic state $X(^2\Pi)$ vs. the internuclear distance in Bohr radii ($a_0 \approx 5.29 \times 10^{-11}$ m) [8, 18]. Blue lines indicate the vibrational states ν of the electronic ground state [19].

Hydrogen chloride (HCl) is such a molecule. It is a small, diatomic molecule and it's two most abundant isotopes, $H^{35}Cl$ with a natural abundance of 76 % and $H^{37}Cl$ with 24 %, are stable [19]. It is commercially available and is relevant for combustion processes, especially of biomass [20] or polyvinyl chloride compounds [21]. Furthermore, it has an absorption band at a wavelength of 3.5 µm, which lies within the output wavelength of an optical parametric oscil-

lator (OPO) available in our lab. There are also detectors available for the third harmonic at 1.17 µm.

For resonance enhancement, we need HCl's energy states and the transitions among them. Fig. 2.1 shows the electronic ground state X($^1\Sigma^+$), two excited states, and the ionic state of $H^{35}Cl$. The transition between the first excited electronic state A($^1\Pi$) and the ground state has a wavelength of roughly 157 nm (corresponding to a wavenumber of 63 700 cm^{-1}) and a transition dipole moment of 3.14×10^{-30} C m [18]. Even though it is a dissociative state, we have to consider it for the calculation of the nonlinear susceptibility. The transition between the electronic ground state and the bound, excited electronic state C($^1\Pi$) has a wavelength of roughly 129 nm (corresponding to a wavenumber of 77 670 cm^{-1}) and a transition dipole moment of 3.7×10^{-30} C m [18].

As a diatomic molecule, HCl has a single vibrational mode and a single rotational mode. It stretches along the connection axis of both constituents and rotates orthogonal to this axis. Fig. 2.1 shows the vibrational energy levels for the electronic ground state in blue with the quantum number v. The rotational states, with quantum number N, form a fine-structure for the vibrational states. They are omitted in that figure for clarity's sake.

Tab. 2.1 shows the most important molecular parameters of HCl and their corresponding Dunham coefficients in order to calculate the energy of the state with the quantum numbers v, N following the Dunham expansion [22]

$$E(v, N) = \sum_{l,j} Y_{lj} \left(v + \frac{1}{2} \right)^l N^j (N+1)^j. \tag{2.1}$$

The parameters ω_e, $\omega_e x$, and $\omega_e y$ describe the vibration, while the parameters D_e, B_e describe the rotation. The parameter α_e describes a rotational-vibrational coupling. From these parameters, the vibrational transitions have a wavenumber of approximately 3 000 cm^{-1} (3.3 µm) and the rotational transitions have a wavenumber of approximately 11 cm^{-1} (330 GHz or 0.9 mm wavelength). Note that the vibrational transition frequency decreases for larger v due to the anharmonicity.

		$H^{35}Cl$ X($^1\Sigma^+$) [23]	$H^{35}Cl$ C($^1\Pi$) [24]	$H^{37}Cl$ X($^1\Sigma^+$) [25]
T_e	$Y_{0,0}$	0	76092	0
ω_e	$Y_{1,0}$	2990.946	2817.5	2988.660
$\omega_e x$	$-Y_{2,0}$	52.819	66.0	52.720
$\omega_e y$	$Y_{3,0}$	0.224	-	0.218
B_e	$Y_{0,1}$	10.593	9.44	10.577
α_e	$-Y_{1,1}$	0.307	0.15	0.306
D_e	$Y_{0,2}$	5.319×10^{-4}	-	5.301×10^{-4}

Table 2.1: Molecular parameters and corresponding Dunham coefficients $Y_{l,j}$ of HCl in cm^{-1}. We did not find molecular parameters for the excited state C($^1\Pi$) of $H^{37}Cl$.

Due to selection rules, transitions among vibrational states of the same electronic state always change the rotational quantum number ($\Delta N = \pm 1$) as well. These rovibrational transitions have transition dipole moments of 0.2×10^{-30} C m for $\Delta v = \pm 1$,

while the third overtone transitions have dipole moments of 0.001×10^{-30} C m [19].

The population of the energy states follows the normalized Boltzmann distribution, given by

$$p(v, N) = \frac{1}{Z} \exp\left(-\frac{E(v, N)}{k_B T}\right), \tag{2.2}$$

with the energy E, the partition function $Z = \sum_{v,N} p(v, N)$, the Boltzmann constant k_B, and the temperature T. At room temperature, mainly the vibrational ground state $v = 0$ is populated, while multiple rotational substates are populated. For $H^{35}Cl$, the most populated rotational state is $N = 3$, comprising approximately 19 % of the total molecular population.

2.2 Mid-Infrared Seed Source

For resonantly enhanced THG and SFM in HCl, we need a laser system tunable over a few nanometers around a wavelength of 3.5 µm, with a peak output power of more than 1 kW to compensate the small nonlinear susceptibility of a few pm^2/V^2, and with a bandwidth of less than 1 GHz in order to resolve individual resonances. This implies a pulse duration of more than 1 ns. At room temperature, the Doppler broadening is approximately 170 MHz (FWHM), so a laser linewidth on that order is acceptable.

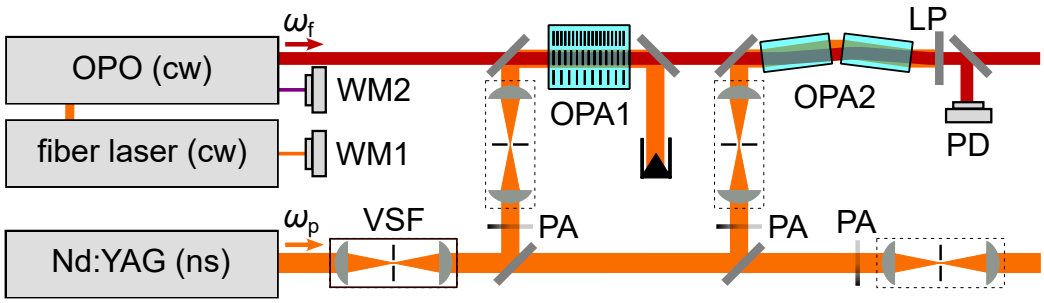

Figure 2.2: Setup of the laser system with wavemeters (WM), vacuum spatial filter (VSF), attenuators made of lambda/2 plate and polarizer (PA), pre-amplifier (OPA1), power amplifier (OPA2), longpass filter (LP), and photodiode (PD). The top beam serves as fundamental radiation and the bottom one is used for SFM.

Fig. 2.2 presents an overview of the laser system, which includes an OPO coupled with an optical parametric amplifier (OPA). An external fiber laser oscillator (Koheras Basik Y10, NKT Photonics) with a fiber amplifier (YAR-15K, IPG Photonics) provides up to 15 W pump radiation for the OPO with a wavelength of 1 064 nm and a tuning range of 200 GHz. The commercially available, continuous-wave (CW) OPO (Argos 2400-C, Aculight) produces mid-infrared (idler) radiation ω_{idler} in the wavelength range 3.2–3.9 µm with a power around 1 W. Its cavity is resonant for the signal radiation ω_{signal} only and contains an intra-cavity etalon to prevent the signal to hop between different longitudinal modes. Consequently, the idler frequency follows the frequency tuning of the OPO's pump laser at ω_{pump}. Two wavemeters (WM1 and WM2, WS6-600 and WS6-200, High Finesse) measure the wavelengths of the fiber laser oscillator and of the OPO's signal radiation, respectively. We determine the idler radiation with $\omega_{idler} = \omega_{pump} - \omega_{signal}$.

2.3 Amplifier Pump Source

A Q-switched Nd:YAG laser (Pro 230, Spectra Physics) produces (ns) pulses with a wavelength of 1 064 nm, a pulse energy of 1.1 J, and a pulse duration of 8 ns (FWHM) at a repetition rate of 20 Hz. An injection-seeder (ROCK fiber laser, NP Photonics) enables single longitudinal mode operation in the Nd:YAG laser, resulting in a smooth temporal pulse profile with a Fourier limited bandwidth of 55 MHz (FWHM).

We recorded the temporal pulse shape with an ultra-fast photodiode (UPD-200-UD, Alphalas, rise time: < 175 ps, bandwidth: > 2 GHz), sampled by a digital oscilloscope (WaveRunner 104Xi, Le Croy) with a bandwidth of 1 GHz. Figs. 2.3 (a) and 2.3 (b) show the temporal pulse shapes with and without the injection-seeder. Without the injection-seeder, a pulse starts 10 ns later than with the seeder as the pulse requires more time to build up in the laser cavity [26]. The temporal pulse shape without the seeder contains fluctuations. Diaz *et al.* noticed that these fluctuations are significant spikes, sometimes several times larger than the maximum power during seeded operation, and that the bandwidth broadens to 20 GHz (FWHM) [27]. The rise-time of the photodiode and the bandwidth of the oscilloscope smooth the spikes, with a duration of a few picoseconds, to small fluctuations at nanosecond timescale.

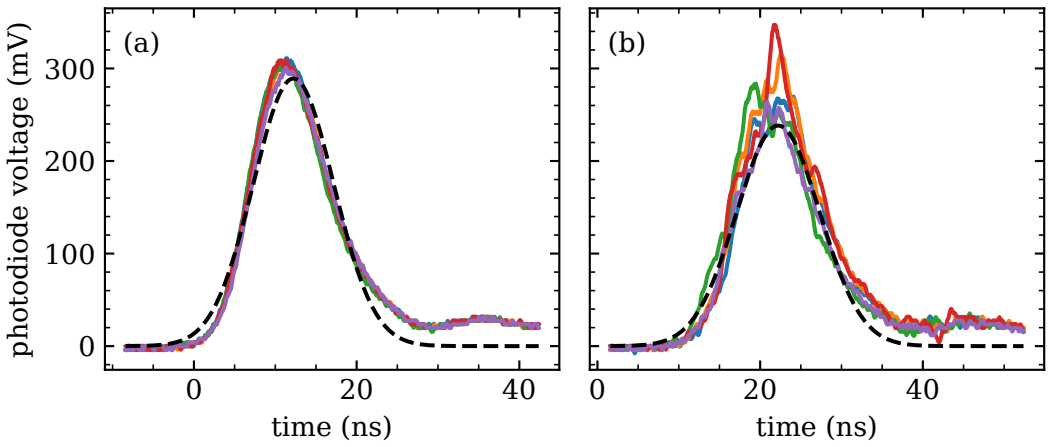

Figure 2.3: Ultra-fast photodiode signal vs. time for 5 consecutive Nd:YAG pulses (a) with and (b) without seed laser enabled. The dashed black line indicates a Gaussian fit to one of the traces. The seeded pulses arrive 10 ns earlier and exhibit less fluctuations than the unseeded ones.

The laser is placed on a different optical table and the beam profile deteriorates over the long propagation distance of several meters. A spatial filter (VSF) removes higher modes from the beam in order to improve the beam profile towards a Gaussian profile. It consists of an anti-reflective (AR)-coated UVFS lens combination with an effective focal length of 2 m, a pinhole, and another AR-coated N-BK7 lens combination with an effective focal length of 1.7 m. The high fluence in the higher modes would slowly erode commercially available pinholes. Therefore, the pinhole is a home-built, stainless steel, 6.55 mm thick disk with a hole of decreasing diameter, from 1.0 mm on the entrance side to 0.8 mm on the exit side. Fig. 2.4 shows a cut view. The thickness of the pinhole allows to absorb many shots without dete-

riorating performance. The even higher fluence in the center ignites plasma in air, which not only deforms the beam profile, but also damages the pinhole. Therefore, we placed the pinhole in a 3 m long vacuum tube with AR-coated windows at both ends. Flexible vacuum tubes on both sides of the pinhole ensure alignability of the pinhole without moving the whole setup. For more details see Ref. [28].

A set of beamsplitting mirrors (70 % reflection, 30 % transmission, BST11, Thorlabs) split the radiation into different arms, one for each of the two amplifier stages and one for the spectroscopic measurement itself. Each arm contains an attenuator (PA), made of a motorized half-wave plate (2-CPW-ZO-L2-1 064, Altechna) and a polarizing beamsplitter (2-HPCB-C-0125, Altechna), in order to control the pulse energy in that arm.

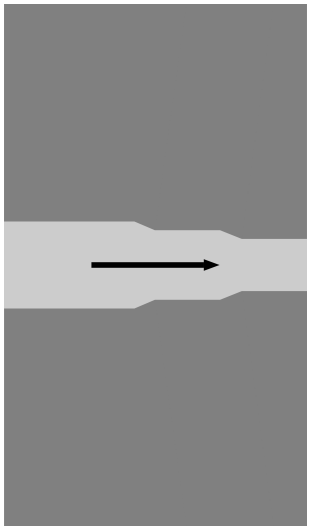

Figure 2.4: Cut of the home-built pinhole along beam propagation (adapted from Ref. [28]). The arrow indicates the beam propagation. The pinhole is 6.55 mm thick. The hole diameter (transverse to beam propagation) is 1000 µm on the entry side, 900 µm in the middle, and 800 µm on the exit side.

2.4 Pre-Amplifier

A periodically poled lithium niobate (PPLN) crystal (HC Photonics) is used as an OPA for the CW mid-infrared radiation. The crystal is 50 mm long with a $12 \times 1\,\mathrm{mm}^2$ aperture and is anti-reflection coated for all interacting fields. Distributed along the 12 mm aperture axis are seven tracks, each with a distinct phase-matching poling period ranging from 27.17 to 30.45 µm. 5 % Magnesium Oxide (MgO) doping prevents photorefractive effects. A PID-regulated oven (TC038, HC Photonics) controls the crystal temperature from room temperature up to 200°C. This temperature control, combined with various poling periods, enables quasi-phase-matching for optical parametric amplification across a wavelength range of 3.2–4.6 µm. For our experiments with HCl, we used the track with a 29.8 µm poling period, providing quasi-phase-matching for a spectral range of 3.44–3.71 µm.

An uncoated CaF_2 lens with a 50 mm focal length focuses the (cw) mid-infrared radiation into the crystal, producing a beam waist ($1/e^2$ radius) of 300 µm and a confocal parameter of 10 cm. We used a home-built beam profiler to determine the mid-infrared beam profile. The setup samples the pulse energy at various transverse positions with a small aperture (typically 50 µm diameter) and an InAsSb photodiode (P13243-011MA, Hamamatsu), both mounted on a motorized, two-dimensional translation stage.

A spatial filter, made of a 150 µm diameter pinhole (HP-3/8-DISC-DIM-150, Lenox Laser) between two AR-coated N-BK7 lenses with 500 mm (LA1908-YAG, Thorlabs) and 60 mm (LB1596-B, Thorlabs) focal lengths filters the pump pulses of the Nd:YAG and reduces their beam radius. Within the crystal, the collimated pump pulses have a radius ($1/e^2$) of 425 µm. With this configuration, a pulse energy of 1.5 mJ reaches the damage threshold of $1\,\mathrm{J/cm}^2$, so the maximum pump pulse energy is limited to 0.75 mJ, including a safety margin.

Dielectric mirrors (Laseroptik, highly reflective (HR)-coated at 1 064 nm and highly transmissive (HT)-coated at mid-infrared wavelengths) are used to combine and later separate the mid-infrared seed beam and the pump beam before and after the pre-amplifier. Following this, a CaF_2 lens collimates the mid-infrared pulsed beam. The pre-amplifier generates mid infrared pulses with a pulse energy of 37 µJ for a seed power of 0.96 W and a pump pulse energy of 670 µJ.

2.5 Power Amplifier

The radiation from the pre-amplifier is further amplified in a second OPA stage (OPA2) made of bulk lithum niobate (LNB) crystals. This approach is necessary because producing PPLN crystals with a thickness greater than 1 mm is not feasible, and PPLN cannot tolerate much higher pump fluences. A long-pass filter (No. 68653, Edmund Optics) between both OPA stages blocks the signal radiation of the first OPA stage to prevent back conversion.

This second OPA stage consists of two 3 cm long LNB crystals (Castech) in walk-off-compensating configuration as described in Ref. [29]. These crystals are also doped with 5 % MgO, have anti-reflection coatings for the relevant wavelengths, and are cut for type I critical phase-matching with cutting angles $\theta = 45°$ and $\phi = 30°$. The end facets are cut with a 0.5° wedge to prevent an etalon effect, which arises from multiple internal reflections interfering with each other in plan-parallel geometry.

We monitor the idler pulse energy with an InAsSb photodiode (PD, P13243-011MA, Hamamatsu) calibrated with an energy meter (PE10-C, Ophir). Stepper motors allow to constantly adjust the phase-matching angle during changes in wavelength (see Appendix C). Dielectric mirrors (Laseroptik, HR-coated at 1 064 nm and HT-coated at mid-infrared wavelengths) combine the seed and pump beams and separate them again. Due to production error, their damage threshold is at 2 J/cm^2 (10 ns pulses at 1 064 nm), limiting the pump pulse energy to 25 mJ.

In this power amplifier, both the pump and seed beams are collimated with ($1/e^2$) radii of 0.8 and 1.95 mm, respectively. The spatial filter for the pump pulses consists of a 500 µm pinhole (HP-3/8-DISC-DIM-500, Lenox Laser) between two AR-coated N-BK7 lenses of 750 mm (LA1978-YAG, Thorlabs) and 300 mm (LA1484-B-ML, Thorlabs) focal lengths. For a typical pump pulse energy of 23 mJ, the mid-infrared pulse energy is up to 1.7 mJ.

2.6 Mid-Infrared Pulse Characterisation

Let us turn our attention to the characterisation of the laser system and the generated mid-infrared pulses. We measured the idler power of the Aculight OPO, which acts as the mid-infrared seed for the OPA chain, with a power meter (3A, Ophir). As shown in Fig. 2.5 (a), the seed power decreases with increasing wavelengths, from 1.6 W at 3270 nm to 0.7 W at 3770 nm, consistent with the manufacturer's specification. This decrease is partly due to the growing absorption in the OPO's nonlinear medium, LNB, beyond 3500 nm [30]. The pulse energy of the pre-amplifier's nanosecond

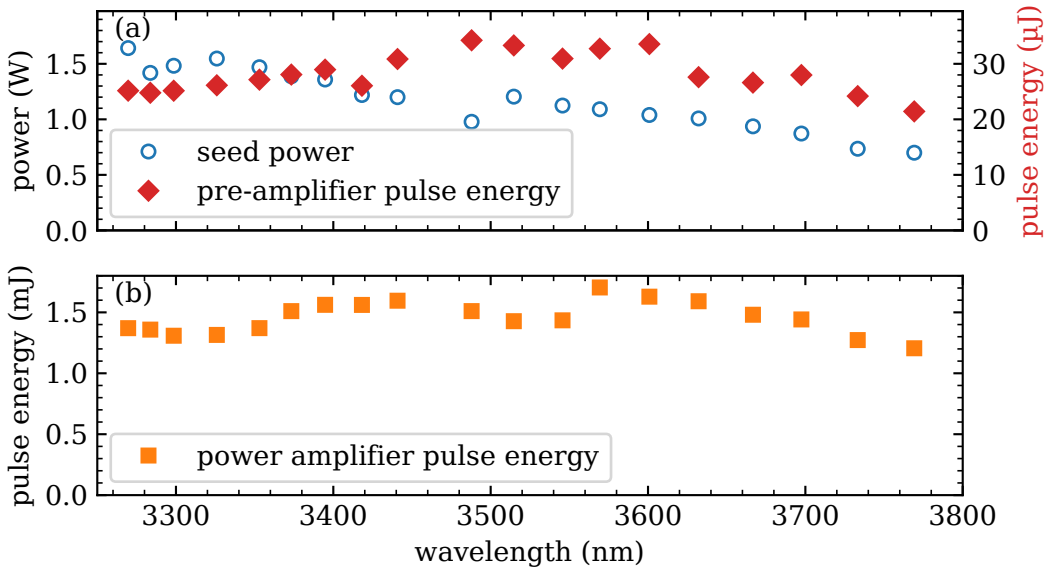

Figure 2.5: (a) Mid-infrared seed power and pre-amplifier pulse energy, and (b) power amplifier pulse energy vs. wavelength. In (a), hollow blue circles represent the seed power (left axis) and filled red diamonds represent the pre-amplifier pulse energy (right axis). The pump pulse energy was 500 µJ for the pre-amplifier and 22.9 mJ for the power amplifier. Adapted from Ref. [17].

pulses, measured with a pyroelectric energy meter (PE10-C, Ophir), also diminishes from over 30 µJ to 20 µJ for wavelengths above 3500 nm.

Fig. 2.5 (b) shows that after passing through the power amplifier, the pulse energy continues to decrease as the wavelength increases, reaching a peak of 1.7 mJ at 3570 nm and falling to 1.2 mJ at 3770 nm. Nevertheless, the mid-infrared pulse energy remains above 1 mJ across the 3270–3770 nm tuning range.

In addition to the pulse energy, the pulse duration and bandwidth are relevant for nonlinear spectroscopy. Since direct measurements of the duration of mid-infrared pulses were not possible, we up-converted the power amplifier's signal radiation at 1520 nm to 760 nm via second harmonic generation (SHG) in an uncoated 12 mm long beta-barium borate (BBO) crystal (Castech). An ultra-fast photodiode (UPD-200-UD, Alphalas) detected the temporal profile of the SHG signal, and a 1 GHz bandwidth oscilloscope (Waverunner 1X04i, LeCroy) sampled the signal, yielding a Gaussian-shaped profile with a FWHM of 4.2 ns. After accounting for the 1 ns time constant of the detection setup, including photodiode rise time and oscilloscope bandwidth, we deduced a pulse duration of 4.1 ns for the SHG pulses and 5.8 ns for the signal radiation. Given the large amplification in the power amplifier, we assume the mid-infrared idler radiation has the same 5.8 ns pulse duration.

Lastly, we assessed the bandwidth of the mid-infrared radiation using absorption spectroscopy in HCl. The collimated mid-infrared beam was transmitted through an 18 cm long gas cell with uncoated, wedged CaF_2 windows (WW51050, Thorlabs) at an HCl pressure of 0.09 mbar. At this pressure, Doppler broadening dominates the spectral lines of HCl, resulting in a Gaussian profile with a linewidth of 175 MHz (FWHM). We will provide more details on the gas setup and spectral lines later. To quantify transmission, calibrated InAsSb photodiodes (P13243-011MA,

Hamamatsu) measured the pulse energy before and after the gas cell. Fig. 2.6 shows the absorption coefficient while tuning the mid-infrared wavelength around the one-photon resonance of $H^{37}Cl$ at 3546.65 nm (P-branch, $N = 3 \rightarrow 2$) for both CW radiation from the OPO and mid-infrared pulses generated by the power amplifier.

A Gaussian fit to the CW measurement yields a linewidth of 190 MHz (FWHM), consistent with the expected linewidth for an HCl spectral line at this pressure. Given that the CW OPO has a bandwidth of less than 1 MHz, its contribution to the overall linewidth is negligible. By deconvoluting the 219 MHz linewidth measurement for the nanosecond pulses with the spectral linewidth of HCl, we calculate a laser bandwidth of 108 MHz for the mid-infrared ns pulses [17]. With a pulse duration of 5.8 ns, this results in a time-bandwidth-product of 0.63, which is reasonably close to the Fourier limit of 0.44 for Gaussian pulses.

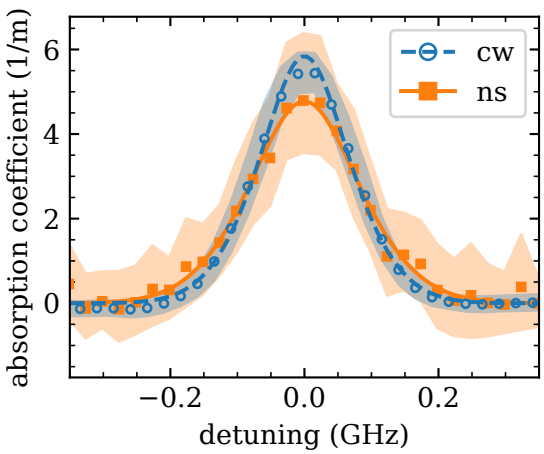

Figure 2.6: Absorption coefficient vs. detuning from a one-photon resonance of $H^{37}Cl$ at 3546.65 nm with CW and ns radiation. Markers, hollow blue circles for CW and filled orange squares for ns, represent frequency binned data points, while the shaded area indicates standard deviation. The solid orange line and dashed blue line represent Gaussian fits to the measurement data, respectively. The HCl pressure was 0.09 mbar. Adapted from Ref. [17].

In summary, the laser system emits mid-infrared pulses with a pulse energy of more than 1 mJ across a tuning range of 3270-3770 nm at a 20 Hz repetition rate. The pulses have a pulse duration of 5.8 ns and are almost Fourier limited with a time-bandwidth-product of 0.63.

Chapter 3

Resonantly Enhanced SFM vs. THG via Molecular Resonances

We turn now to the experimental demonstration and investigation of resonantly enhanced THG and SFM spectroscopy via rovibrational states in HCl. With these results, we will discuss the advantages and disadvantages of both methods. We published the main results in "Physical Review A" [31].

3.1 Simulation of Resonantly Enhanced THG and SFM in HCl

Having introduced the test gas HCl and our laser system, we can resume the calculation of the nonlinear susceptibility and expected signal power for resonantly enhanced THG and SFM in HCl.

3.1.1 Simulation Parameters

We applied Eqs. 1.1, 1.2, and 1.3 to calculate the expected output power, nonlinear dielectric susceptibility, and phase-matching integral, respectively, for the processes of THG and SFM in HCl.

The calculation of the nonlinear susceptibility, as defined in Eq. 1.2, involves summing over all possible transition paths, which are sets of any three quantum states. Figs. 3.1 (a,b) show two such transition paths (their states are marked with bold lines) for the same isotope, $H^{35}Cl$, and the same fundamental frequency, ω_f. However, many transition paths have negligible contributions due to factors as forbidden transitions, unpopulated ground states, or excessively large detunings. To optimize computational efficiency, it is crucial to exclude these insignificant transition paths, as their inclusion only increases the computation time without significantly affecting the results.

Previous simulations for THG restricted transition paths to those involving rovibrational states of the electronic ground state, like the path shown in Fig. 3.1 (a), which exhibit small detunings and were believed to dominate the nonlinear response [8]. However, discrepancies between the simulation and experimental results prompted reevaluation. We expanded our model to include transition paths that incorporate the excited electronic state $|e\rangle$, as shown in Fig. 3.1 (b). To quantify the impact of these additional transition paths on both the nonlinear susceptibility and THG power, we performed the calculation twice — once excluding and once including the electronic state. The simulation of SFM uses the same transition paths, only the resulting detunings differ, for example Figs. 3.1 (b,c) show the same transition path applied to both processes.

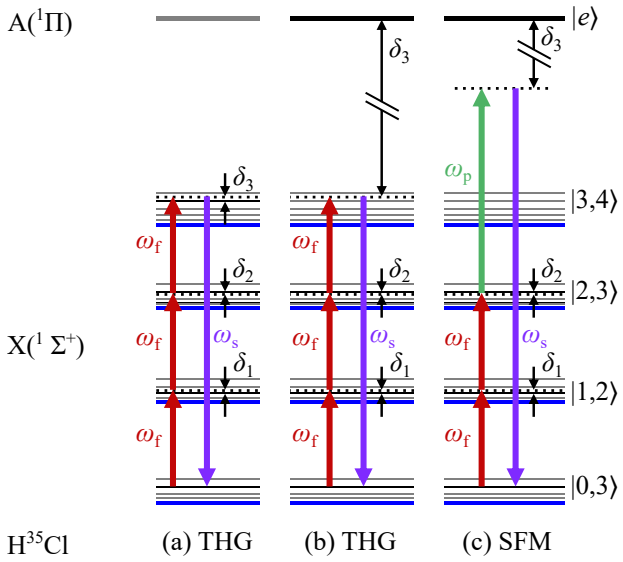

Figure 3.1: Level scheme of $H^{35}Cl$ with transition paths for (a) THG among rovibrational states, (b) THG involving an excited electronic state, and (c) SFM. The transition paths are close to a two-photon transition ($\delta_2 \approx 0$) for a fundamental wavelength of 3 533.12 nm (ω_f). Dotted lines represent the photon energy, while bold lines highlight the rovibrational state used for detuning δ_i in the respective configuration.

The HITRAN database offers spectroscopic information regarding rovibrational transitions: quantum numbers, transition frequencies, linewidths, broadening parameters, and transition dipole moments [19]. Eq. 2.2 allows to calculate the population of the different states for a given temperature. However, HITRAN does not provide data for electronic transitions. Due to the large detuning from the excited electronic states, it is justified to approximate the manifold of rovibronic transitions between the electronic states $A(^1\Pi) \leftarrow X(^1\Sigma^+)$ by a single transition. We calculate three-photon detunings and transition dipole moments from parameters given in Ref. [18]. The relevant detunings to the excited electronic state are $\delta_3(\mathrm{THG}) = 55\,228\,\mathrm{cm}^{-1}$ for THG and $\delta_3(\mathrm{SFM}) = 48\,661\,\mathrm{cm}^{-1}$ for SFM. From spectroscopic data in Ref. [18] we estimate electronic transition dipole moments in the range of $\mu_{e2} \approx \mu_{e0} = 3.14 \times 10^{-30}\,\mathrm{C\,m}$ for both THG and SFM.

Eq. 1.2 depends on the dephasing rates γ of the involved transitions, which are determined by the natural linewidth and various broadening mechanisms. All parameters used are sourced from the HITRAN database. The natural linewidth for vibrational transitions is typically only a few Hz, but molecular collisions broaden the linewidth, with a broadening rate proportional to the gas pressure and scaling factors on the order of MHz/mbar [19]. Both the natural linewidth and collisional broadening result in a Lorentzian line shape [15]. In contrast, the Doppler effect introduces Gaussian broadening, which depends on temperature and molar mass, but is independent of pressure. For HCl at room temperature, Doppler broadening is 88 MHz (half width at half maximum (HWHM)) [19]. The overall lineshape is modeled as a Voigt profile, the convolution of the Gaussian Doppler broadening and the Lorentzian broadening of the natural linewidth due to collisions [32]. At low pressures ($p \lesssim 50$ mbar), Doppler broadening dominates the linewidth. However, as pressure increases, collisional broadening surpasses Doppler broadening, reaching a few GHz at 1 000 mbar. For simplicity, we always assume a Lorentzian profile with a HWHM equivalent to that of the Voigt profile, accounting for the natural linewidth, collisional broadening, and Doppler broadening [33].

We restrict the calculation to vibrational states $v \leq 3$ in the sum over transition paths t. This is well justified, as the detunings to higher vibrational states increase

and the transition moments quickly decrease. Moreover, in the sum we consider only transitions obeying the selection rules $\Delta v = \pm 1$ and $\Delta N = \pm 1$.

To compute the phase-matching integral, the refractive indices for all involved waves are necessary. Refs. [34, 35] provide refractive indices of HCl in the mid-infrared and near-infrared regions, respectively. However, these measurements have a resolution of more than 600 GHz, which is insufficient for accurately resolving data near vibrational resonances. Alternatively, the refractive index can be calculated as $n_{\text{sim}} = \sqrt{1+\chi^{(1)}}$, where $\chi^{(1)}$ is the linear susceptibility [15]. While this method, based on transition lines from the HITRAN database, provides high resolution, it underestimates the refractive index, returning values below 1. This discrepancy arises from the omission of contributions from transitions to excited electronic states.

To address this, we combined data from both sources. Fig. 3.2 shows the refractive index for mid-infrared wavelengths around vibrational resonances. The blue plus markers represent the difference Δn between the simulation results and the experimental data from Ref. [34] (denoted by red crosses) at frequencies ω_r centered between two vibrational transitions. The final refractive index is computed by adding the simulation result to this difference, $n = n_{\text{sim}} + \Delta n$, using cubic interpolation (dotted line) between data points for Δn.

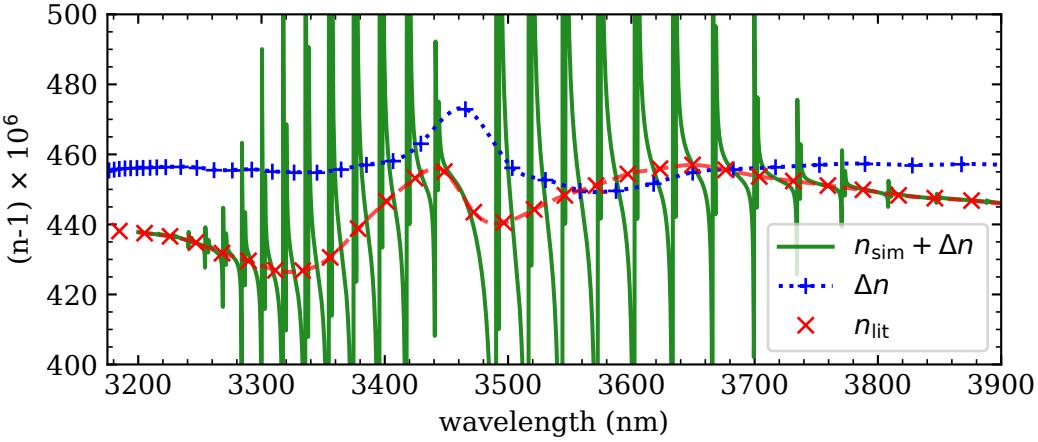

Figure 3.2: Refractive index vs. wavelength for 1013 mbar and 0°C. The red crosses indicate values from Ref. [34]. The blue plus markers represent the difference between the literature values and the simulation at frequencies between two vibrational resonances. The dashed and dotted lines show a cubic interpolation between data points, respectively. The green line is the resulting refractive index n, combining literature and simulation.

By construction, the calculated refractive index n matches the literature values precisely at those frequencies ω_r between resonances. Between these points, the refractive index retains the detailed resonance structure derived from HITRAN lines. This approach effectively merges the slowly varying experimental data with the rapidly fluctuating simulation results.

For different pressures p and temperatures T, the refractive index is

$$n(\omega, T, p) = \sqrt{1+\chi^{(1)}(\omega, T, p)} + \frac{p\,\Delta n(\omega)}{p_{\text{ref}}(1+\alpha T)}, \tag{3.1}$$

with a temperature coefficient of $\alpha = 3.66 \times 10^{-3}\,\mathrm{K}^{-1}$ for HCl [35] and a reference pressure of $p_{\mathrm{ref}} = 1\,013$ mbar. We calculated Δn for standard conditions (1 013 mbar pressure and 0°C).

The setup parameters mirror those used in our experimental configuration. Both the fundamental and, for SFM, probe pulses have a pulse energy of 0.5 mJ and a Gaussian temporal profile with a FWHM of 5 ns. The probe pulses have a wavelength of 1 064 nm. They both have a confocal parameter of 6 cm, with their focal point positioned at the center of the interaction region. This interaction region, an 18 cm long gas cell, contains 30 mbar of HCl (with natural isotopic abundance) at a temperature of 25°C.

See Ref. [36] for the simulation code and documentation of the simulation.

3.1.2 Simulation Results

Eqs. 1.1 and 1.4 describe how the power of both THG and SFM signals depends on the input powers. However, in short-pulse laser systems, pulse energy, rather than power, is typically the measurable quantity. The pulse energy E is the time integral of the power, $E = \int_{-\infty}^{\infty} P(t)\mathrm{d}t$. Assuming that pulses with varying energies have identical temporal profiles, we can express the power as $P_i(t) = E_i \cdot f_i(t)$, where $f_i(t)$ represents the normalized pulse shape.

Integrating Eq. 1.4 and using this form for the input powers gives the SFM pulse energy as $E_{\mathrm{SFM}} \propto \int_{-\infty}^{\infty} P_{\mathrm{f}}^2(t)\,P_{\mathrm{p}}(t)\,\mathrm{d}t = E_{\mathrm{f}}^2\,E_{\mathrm{p}}\,k$, where $k = \int_{-\infty}^{\infty} f_{\mathrm{f}}^2(t)\,f_{\mathrm{p}}(t)\,\mathrm{d}t$ is a pulse shape factor that accounts for the interaction between the different pulse forms, but is independent of the pulse energies. Therefore, for constant pulse shapes, we expect a quadratic dependence on the fundamental pulse energy, $E_{\mathrm{SFM}} \propto E_{\mathrm{f}}^2$, and a linear dependence on the probe pulse energy, $E_{\mathrm{SFM}} \propto E_{\mathrm{p}}$. In contrast, the THG signal pulse energy exhibits a cubic dependence on the fundamental pulse energy.

Fig. 3.3 shows the expected signal pulse energy vs. wavelength for the three simulated processes: THG considering only the vibrational states of the electronic ground state, THG considering also the excited electronic state, and SFM. It is clearly visible that the excited electronic state is relevant for THG, as it increases the maximum signal pulse energy by two orders of magnitude from 1.6 pJ to 272 pJ. These signal pulse energies are tiny compared to the 0.5 mJ fundamental pulse energy due to the low density of a gas, especially at the reduced pressure of 30 mbar. The spectra, however, are still similar.

The large dipole moments of transitions to the excited electronic state are the reason for the large difference of generated signal pulse energy. Tab. 3.1 compares the dipole moments and detunings of two transition pathways shown in Fig. 3.1. Both start at the state $|v = 0, N = 3\rangle$ of $\mathrm{H}^{35}\mathrm{Cl}$ and are two-photon resonant to $|v = 2, N = 3\rangle$ at a fundamental wavelength of 3 533.12 nm. One pathway couples the third transition to the vibronic state $|v = 3, N = 4\rangle$ of the electronic ground state, while the other couples to the excited electronic state $\mathrm{A}(^1\Pi)$, indicated by $|\mathrm{e}\rangle$. The merely rovibronic pathway's three-photon detuning of $79\,\mathrm{cm}^{-1}$ is almost three orders of magnitude smaller than the $55\,101\,\mathrm{cm}^{-1}$ detuning to the electronic state. However, the product $\mu_{32} \cdot \mu_{30}$ of the transition dipole moments of the transitions to and from the third excited state differ by more than four orders of magnitude. According to Eq. 1.2, the contribution of the electronic pathway to the nonlinear

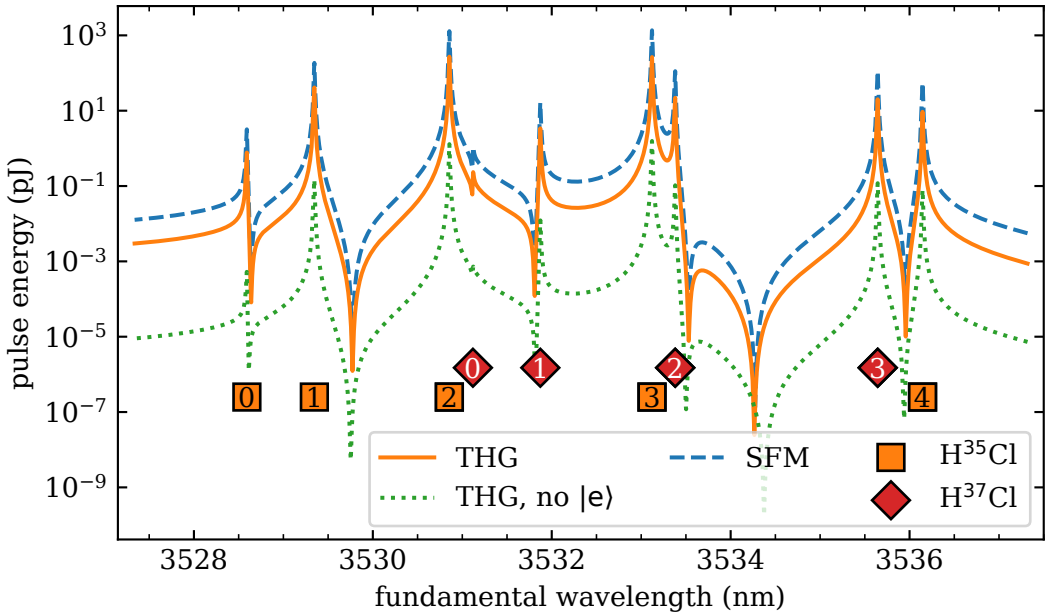

Figure 3.3: Simulated signal pulse energy vs. fundamental wavelength for different nonlinear processes. The dashed blue line represents SFM, the solid orange line THG, and the dotted green line THG ignoring the excited electronic state. Markers indicate the central wavelengths of rovibrational two-photon resonances ($v = 0 \rightarrow 2$, Q-branch with $\Delta N = 0$ in the electronic ground state), with rotational quantum numbers N of the ground state for the transition (orange squares for $H^{35}Cl$, red diamonds for $H^{37}Cl$). HCl pressure is 30 mbar. Note the logarithmic scale on the pulse energy axis.

susceptibility is more than one order of magnitude larger than that of the rovibronic pathway. The signal power depends on the square of the nonlinear susceptibility (see Eq. 1.1), which explains the two orders of magnitude difference in the signal pulse energy.

The SFM process generates a maximum signal pulse energy of 1 361 pJ at a signal wavelength of 664 nm, surpassing THG by almost an order of magnitude. The SFM pathway for aforementioned two-photon resonance is similar to the THG one, which considers the excited electronic state. However, it profits twofold from the higher energy of the probe photons. First, the reduced three-photon detuning (by 6 600 cm^{-1}) increases the nonlinear dielectric susceptibility by 12 %. Second, the probe frequency is more than three times higher than the fundamental one and the signal frequency is more than 1.8 times higher than that of THG, which leads to a six-fold increase of the generated energy (Eq. 1.1).

It is also possible to use probe photons with more energy, for example the second harmonic at 532 nm. Assuming the same pulse energy of 0.5 mJ, the signal pulse energy of 4 400 pJ would be three times larger. However, the required second harmonic generator introduces more complexity and reduces the available probe power.

As detectors for low intensities typically detect the number of photons, not the pulse energy, we have to compare the number of generated photons. The THG pulse contains 1.6 billion photons, the SFM pulse (with a probe of 1 064 nm wavelength) 4.5 billion, and the SFM pulse with a 532 nm wavelength probe beam con-

third excited state	$\|3,4\rangle$	$\|e\rangle$
μ_{32} in 10^{-30} C m	0.256	3.0
μ_{30} in 10^{-30} C m	0.0013	3.0
δ_3 in cm^{-1}	-79.0	55 101
example	(a)	(b)

Table 3.1: Selected parameters for Eq. 1.2 for two THG transition paths with the same first two transitions $|v = 0, N = 3\rangle \rightarrow |1,2\rangle \rightarrow |2,3\rangle$. One transition path contains the rovibrational state $|v = 3, N = 4\rangle$ as the third excited state and the other one contains the excited electronic state $|e\rangle$, see figure (a,b) to the right or Fig. 3.1. Other parameters (for all transitions) are $\delta_1 = -8.79\,cm^{-1}$ and $\mu_{10} \approx \mu_{21} \approx 0.2 \times 10^{-30}$ C m.

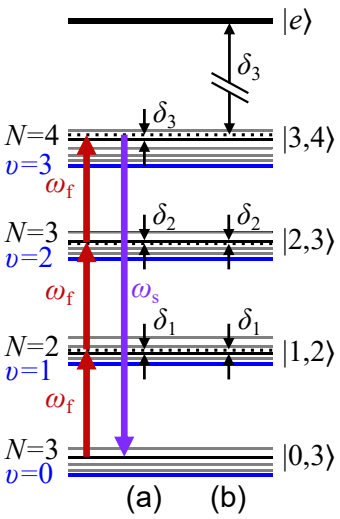

tains 9 billion photons. In this metric, the advantage of SFM (or even SFM with a 532 nm probe) over THG is still present, but not as pronounced as in the energy comparison.

Figs. 3.4 (a,b) show the molecular contributions to the pulse energy, that is the nonlinear susceptibility and phase-matching integral, vs. the fundamental wavelength. The nonlinear susceptibility is nearly identical for SFM and THG with 142 and 138 pm^2/V^2, at least if we consider electronic transitions for THG. For THG ignoring the excited electronic state, it would be only 11 pm^2/V^2. While the phase-matching integral is lower for SFM, the difference is only a factor of two, which alone does not account for the difference of generated photons. However, the number of generated photons depends also on the input frequencies. Since the probe frequency ω_p (for a probe wavelength of 1 064 nm) is more than three times larger than the fundamental frequency ω_f, the number of generated photons is correspondingly more than three times greater.

Let us now turn our attention to the pressure dependence. Figs. 3.5 (a-d) show the different factors of Eq. 1.1 for THG and SFM at various pressures at the two-photon resonance at 3 533.12 nm. The imaginary part of the wave vector mismatch Δk, see Fig. 3.5 (a), is almost negligible for both processes, as the two-photon resonance is far from one-photon resonances (more than 100 GHz) and their absorption. The real part, on the other hand, is proportional to the pressure, as the refractive index scales linearly with the pressure. Also, its slope is larger for SFM than for THG, which influences the phase-matching integral. As Fig. 3.5 (c) shows, the phase-matching integral decreases for increasing pressure, but shows side peaks as expected from the numerical analysis in Sec. 1.1. Due to SFM's larger wave vector mismatch, the phase-matching integral increases faster than for THG and the side peaks appear earlier — the first one appears at 400 mbar, while the first THG side peak appears at 700 mbar.

On the other hand, the nonlinear susceptibility increases linearly with the pressure up to 30 mbar and stagnates then. The pressure dependent factors of the nonlinear susceptibility $\chi^{(3)}$ in Eq. 1.2 are the number density ρ and the dephasing rates γ_i. For an ideal gas, the number density is proportional to the pressure p, such that

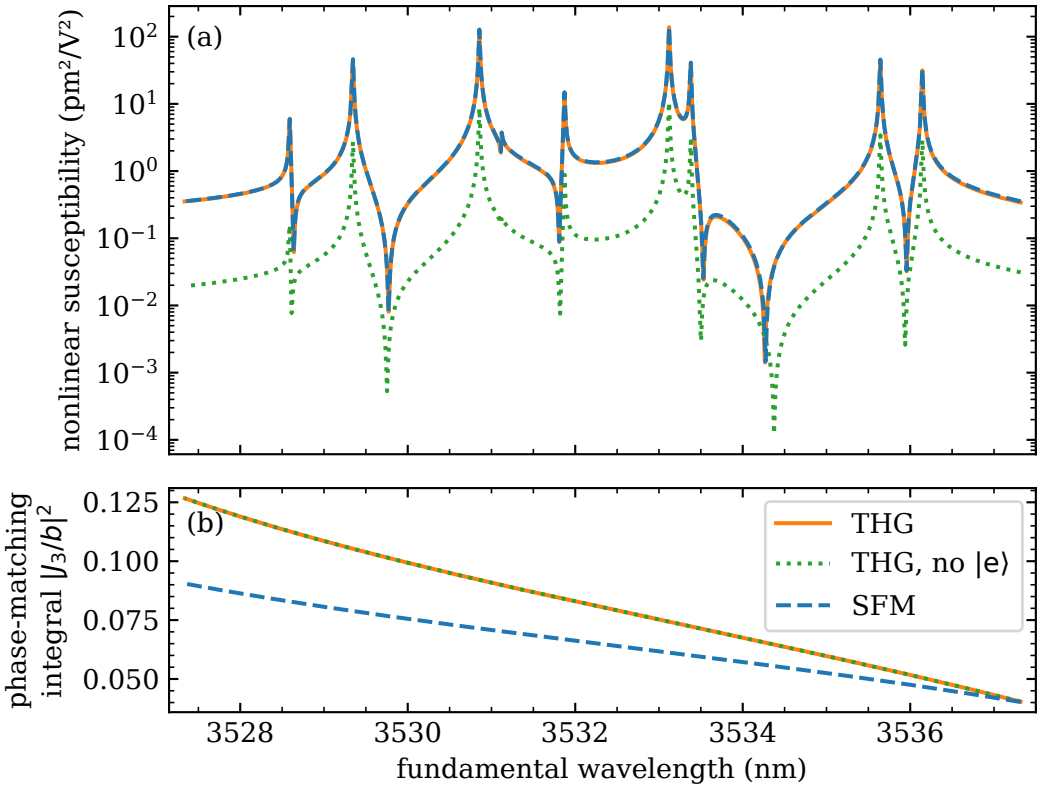

Figure 3.4: (a) Nonlinear susceptibility $\chi^{(3)}$ and (b) square of phase-matching integral divided by the confocal parameter $|J_3/b|^2$ vs. fundamental wavelength for the processes THG (solid orange line), THG ignoring electronic states (dotted green line), and SFM (dashed blue line). Note the logarithmic axis for the nonlinear susceptibility.

$\chi^{(3)} \propto p$. The influence of the dephasing rates γ_i depends on the corresponding detuning δ_i. If the detuning is several ten GHz, then the dephasing rate of less than a GHz — for pressures below 1 000 mbar — barely influences the nonlinear susceptibility. However, for the resonant term ($\delta_i \approx 0$), the nonlinear susceptibility is inverse proportional to the dephasing rate, resulting in $\chi^{(3)} \propto \frac{p}{\gamma_i}$. For low pressures, the dephasing rate is dominated by the pressure independent Doppler broadening, as previously discussed, and thus almost constant, such that $\chi^{(3)} \propto p$. For larger pressures of several ten mbar, collisional broadening dominates and the dephasing rate becomes proportional to the pressure, and thus the nonlinear susceptibility becomes constant.

The nonlinear susceptibility is almost equal for both processes over the whole pressure range, as we already discussed.

The signal pulse energy depends on the product of the square of the phase-matching integral and the square of the nonlinear susceptibility. Consequently, the signal pulse energy in Fig. 3.5 (d) shows a combination of the features of the Figs. 3.5 (b) and (c). It increases with $E \propto p^{1.85}$ for low pressures p, as the phase-matching integral decreases while the square of the nonlinear susceptibility increases quadratically with the pressure. Once the nonlinear susceptibility stagnates at 20 mbar, the phase-matching integral with its oscillations dominates the features of the generated

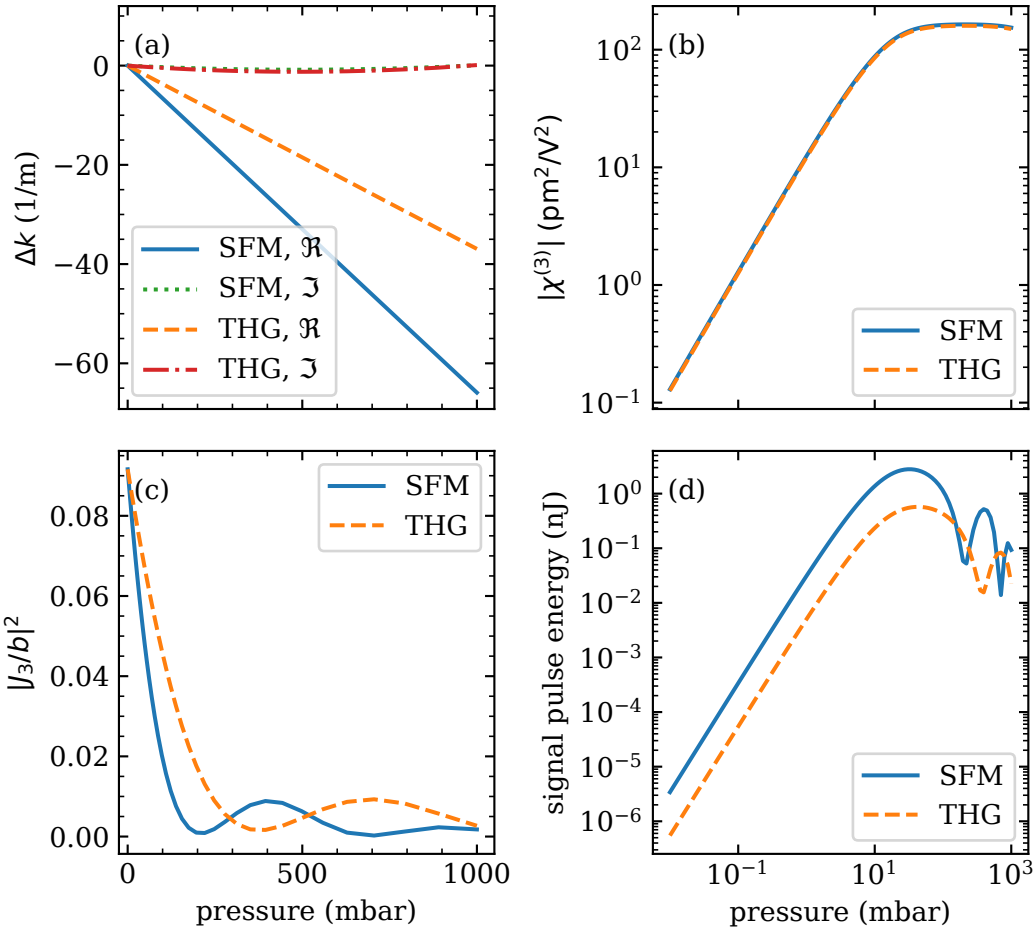

Figure 3.5: (a) wave vector mismatch, (b) absolute value of the nonlinear susceptibility, (c) square value of the phase-matching integral divided by the confocal parameter, and (d) signal pulse energy vs. HCl pressure for a fundamental wavelength of 3 533.12 nm. The solid blue line represents SFM and the dashed orange one THG. In (a), they indicate the real part, while the dotted green line and dashed-dotted red line indicate the corresponding imaginary parts. Note the logarithmic scale on both axes of (b) and (d).

signal pulse energy.

3.2 Experimental Setup

We performed our experiments in a 18 cm long gas cell with uncoated CaF_2 windows (WW51050, Thorlabs) with a 0.5° wedge to prevent an etalon effect.

In previous works, the windows of a 5 cm gas cell generated off-resonant background signal, which reduced the SNR for THG measurements by almost an order of magnitude [8, 37]. Therefore, we increased the cell length to 18 cm in order to increase the spot size of the fundamental beam on the windows and thus reduce the background signal. A combination of a piezo sensor and a Pirani sensor (VCR, Thyracont) measures the pressure inside the cell. A mixing panel with needle valves allows us to evacuate the cell or to fill it with HCl or nitrogen (N_2) at variable flow rates. The HCl gas samples (supplied by Westfalen) have a purity of 99.5 % and a

residual moisture of < 50 ppm.

3.2.1 Wavelength Measurement

We acquired the wavemeter WM2 (see Fig. 2.2 and Sec. 2.2), which measures the wavelength of the OPO's signal radiation, only after the experiments presented in this chapter. Therefore, we used an alternative method to determine the signal wavelength in order to calculate the mid-infrared idler wavelength during these measurements. Fortunately, the OPO remains on the same longitudinal mode for its signal radiation over the 200 GHz wavelength tuning range of its pump source (fiber laser oscillator, see Sec. 2.2), making it sufficient to determine the signal wavelength once. First, we used a home-built grating spectrometer to roughly measure the OPO's idler wavelength, ensuring we were near resonance [38]. Next, we conducted a spectroscopic measurement, as described later in this chapter, and compared the results with the expected spectrum (see Sec. 3.1), providing a more accurate wavelength for a detected peak in the spectrum. Finally, we calculated the signal wavelength based on the mid-infrared resonance frequency of that peak and the pump wavelength measured at the same point.

3.2.2 Optical Setup

Fig. 3.6 shows the experimental setup with the gas cell and the detection setup. An AR-coated CaF_2 lens (L_1, LA5012-E, Thorlabs) with a focal length of 150 mm mildly focuses the fundamental beam (mid infrared beam from the power amplifier in Sec. 2.5) into the gas cell. Fig. 3.7 shows the evolution of the fundamental beam radius as it propagates through the gas cell. The beam focus is 10 cm beyond the entry window and, therefore, deviates slightly from the cell center towards the exit window. The beam waist ($1/e^2$ radius) of 183 µm with a confocal parameter of 6 cm results in a peak intensity around 300 MW/cm^2 for a typical pulse energy of 1 mJ.

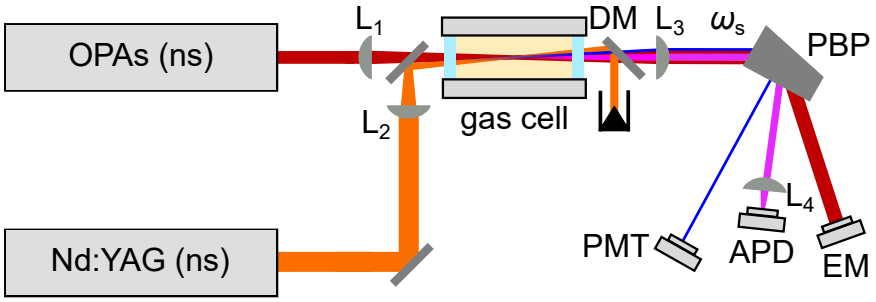

Figure 3.6: Experimental setup for SFM and THG with lenses (L), dichroic mirror (DM), Pellin-Broca prism (PBP), photomultiplier tube (PMT), avalanche photodiode (APD), and energy meter (EM). Note the angle between the beams in the gas cell to indicate a non-collinear geometry.

The laser system also provides a near infrared probe beam at 1 064 nm. A lens system (L_2), consisting of an AR-coated lens with a focal length of 150 mm (LB1437-B, Thorlabs) and an uncoated CaF_2 lens of 250 mm focal length (LA5255, Thorlabs), focuses the probe beam into the gas cell, yielding a focal spot with a beam waist of

55 µm ($1/e^2$ radius) and a confocal parameter of 18 mm. Thus, the peak intensity of the probe beam reaches 2.4 GW/cm^2 at a typical pulse energy of 1 mJ. The beam focus is slightly closer to the gas cell's exit window than to the entry window.

The fundamental and probe beams have parallel, linear polarization. A dichroic mirror (Laseroptik), HR-coated for 1 064 nm and HT-coated for mid-infrared wavelengths, combines the fundamental and probe beams before they enter the gas cell. Due to differences in optical path lengths, the fundamental pulse is delayed by 1 ns relative to the probe pulse at the position of the gas cell. As the pulse durations are 5.8 and 8 ns, respectively, the delay reduces the generated SFM signal only by a few percent.

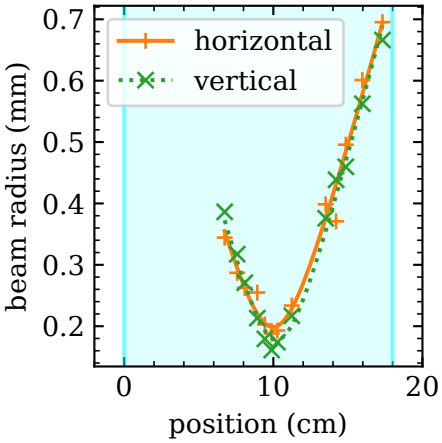

Figure 3.7: Beam radius ($1/e^2$) of the fundamental beam vs. position relative to the cell's entry window. The cyan shaded area indicates the position of the gas cell. Plus and cross markers indicate measurement data, while a solid and dashed line indicate a Gaussian beam fit for the horizontal and vertical beam radii, respectively.

Increasing the cell length to 18 cm reduced the amount of THG in the cell windows. However, they still generated a SFM signal resulting in an increased background level, as we will present later. Hence, we used a slightly non-collinear beam geometry with a small angle of 1° between the fundamental and probe beams to reduce their overlap in the cell windows. For alignment, iris diaphragms were used in front of and after the cell, which were translated by an equal amount in opposite directions, for more details see Ref. [39].

Prior to detection, we separate the SFM signal at a wavelength of 660 nm or the THG signal at a wavelength of 1.2 µm from the intense probe beam with a dichroic mirror (DM, HR-coated for 1 064 nm and HT-coated for mid-infrared wavelengths, Laseroptik). An uncoated CaF_2 lens (L_3, LA5255, Thorlabs) with a 250 mm focal length collimates the signal beams and a CaF_2 Pellin-Broca prism (PBP, ADBV-10, Thorlabs) further separates the signal beams from residual probe and fundamental radiation. The SFM signal passes a bandpass filter (FB650-40, Thorlabs) and is detected by a photomultiplier tube (PMT, R4220, Hamamatsu). The THG signal pulses pass two spectral edgepass filters (FELH1100, Thorlabs; No. 89-675, Edmund Optics) to remove stray light. An AR-coated lens (L_4, LA1608-C, Thorlabs) with a 75 mm focal length focuses the THG signal onto the 200 µm diameter active area of an InGaAs avalanche photodiode (APD, IAG200S6, Laser Components). A translation stage allows precise positioning of the APD's active area to ensure the entire beam is detected.

3.2.3 Detector Setup

Detectors are essential components of any measurement system, especially for detecting low-intensity signals, as expected in our experiments. Commonly used de-

tectors for such applications include PMTs and APDs, both of which rely on the photoelectric effect to generate an electric charge, which is then internally amplified. PMTs utilize the inner photoelectric effect, while APDs use the outer effect. Choosing the right detector can be challenging; for instance, PMTs are not suitable for the mid-infrared regime because their photocathode responsivity typically decreases at longer wavelengths. On the other hand, while APDs can operate in the near-infrared, they offer a much lower internal gain, typically around 10–100, compared to the high internal gain of PMTs, which ranges typically from 10^5 to 10^6.

For the THG signal at a wavelength of approximately 1 178 nm (THG of 3 533 nm), an APD is necessary since no suitable PMT is available for that wavelength range. Despite operating our APD close to its breakdown voltage, its inherent low gain of around 50 requires a transimpedance amplifier (DLPCA-200, Femto) with an amplification factor of 10^6 V/A. However, this setup introduces electronic noise, diminishing the advantage of the APD's high quantum efficiency of 85 %. The amplifier also stretches the pulse duration to several microseconds, allowing our main oscilloscope (Picoscope 4824A, Pico Tech) with a 20 MHz bandwidth to measure the electronic signal accurately. However, this extended integration window also increases susceptibility to background noise. Additionally, the APD's small active area of 200 µm diameter requires precise beam focusing, making alignment more challenging.

For the SFM signal at a wavelength of approximately 664 nm (SFM of 1 064 nm and two times 3 533 nm), PMTs are available. We utilized a PMT, already present in our lab, with a quantum efficiency of 1 % at the signal wavelength. Its high gain of 4×10^6 allows direct voltage measurement with an oscilloscope, bypassing the need for an amplifier and thus avoiding additional electronic noise. The PMT's electric pulses last only a few nanoseconds, hence, they are sampled by an oscilloscope with a 1 GHz bandwidth and 0.2 ns sample time (Waverunner 1X04i, LeCroy). However, the oscilloscope's dead time of 70 ms causes it to miss every other laser shot at a repetition rate of 20 Hz. Due to long delivery times, there were no better suited oscilloscopes available during the time of the experiments in this chapter.

We calibrated both the PMT and APD with attenuated laser pulses at 532 nm (second harmonic of the (ns) Nd:YAG pump laser) and 1 064 nm, respectively. These wavelengths fall within the spectral ranges of the detectors, and the pulse durations are similar to those of the detected signals. Calibrated neutral density filters in front of the THG and SFM detectors attenuate the signal pulse energy as required. This calibration relates the detector signal S to the number of photons N_c in the calibration pulses. We adjust the photon number at signal wavelength N_s to the detector quantum efficiencies η_c and η_s at the calibration and signal wavelengths via the relation $N_s(S) = N_c(S)\,\eta_c/\eta_s$.

3.3 Experimental Results

3.3.1 THG and SFM Spectra

Figs. 3.8 (a) and 3.8 (b) show SFM and THG spectra in HCl at a pressure of 29 mbar, while tuning the fundamental mid-infrared wavelength in the vicinity of rovibra-

tional two-photon resonances. We kept the probe pulse intensity at a comparable level (1.2 mJ pulse energy) to the fundamental pulse intensity in order to permit a "fair" comparison of the SFM and THG spectra. However, much more probe pulse energy would be available from the Nd:YAG laser to further boost the SFM yield.

For fundamental wavelength tuning, we use two modulation methods available to the fiber laser that pumps the OPO. A piezo allows for a fine, triangle modulation with a peak-to-peak range of up to 10 GHz (corresponding to a tuning range of 0.4 nm at a central wavelength of 3 533 nm), while temperature adjustments provide a broader tuning range of up to 200 GHz (8 nm at 3 533 nm). We combine the piezo modulation for precise, slow scanning with the temperature tuning for larger wavelength shifts. The triangle modulation runs continuously, even during the temperature-induced wavelength changes, causing the laser wavelength to vary at different rates depending on their relative phases. This results in uneven data point distribution, with some frequency intervals accumulating more data points and others fewer. To address this, we paused the temperature tuning near expected spectral peaks and in regions where stronger signals were detected, increasing the data coverage in those areas.

Fig. 3.8 (a) also reveals vertical clusters of data points: some below the noise threshold (indicated by the dashed-dotted orange line) and others above it. The PMT, with its low quantum efficiency (less than 1 %) and high gain, produces either no signal, only electronic noise, or a signal distinctly visible on the oscilloscope trace, leading to data points that exceed the dashed-dotted orange line.

The experimental data fit well with the numerical simulation. Note that the logarithmic scale of the signal axes in Fig. 3.8 exaggerates some small deviation in the low intensity wings of the experimentally determined SFM line profile compared to the simulation.

The background is mainly due to electronic noise of the detection setup. Obviously, the noise level in the SFM spectrum is much lower than the one for THG, despite a comparable mean value of the background signal. The larger noise amplitude does not permit observation of the resonance expected at 3 531.87 nm (ground state $N = 1$ in $H^{37}Cl$) in the THG spectrum, while the latter resonance is clearly visible in the SFM spectrum.

When we compare for SFM the weak spectral line at a fundamental wavelength of 3 528.59 nm (ground state $N = 0$ in $H^{35}Cl$) with the strong resonance at 3 533.12 nm (ground state $N = 3$ in $H^{35}Cl$), we find a ratio of 1/400 for their line intensities. Therefore, we expect from Eq. 1.2 to still obtain signal above the noise level down to pressures below 1.5 mbar at the strong resonance. This already indicates the potential of this approach for detection at low pressures, which we will discuss in more detail below. Furthermore, the SNR, i.e., SFM signal level compared to the standard deviation of the background, reaches 4 500 at the strong resonance, which is more than an order of magnitude larger than 190 for THG.

We verified that there is only THG signal and no SFM signal at three-fundamental-photon resonances (outside the depicted wavelength tuning range), as expected for the rather short probe laser wavelength towards a visible SFM signal.

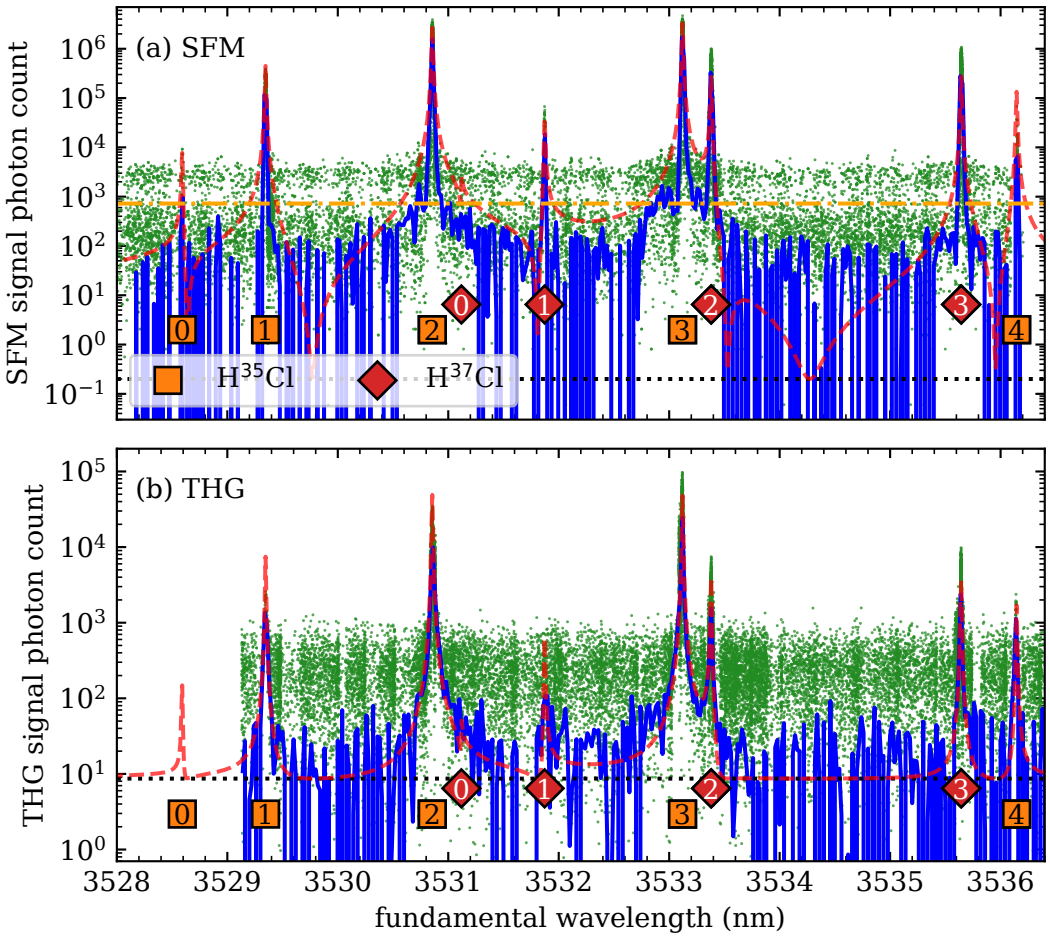

Figure 3.8: (a) SFM and (b) THG signal photon count vs. fundamental wavelength. The fundamental peak intensity was 360 MW/cm^2 (pulse energy 1.2 mJ) for SFM and 300 MW/cm^2 (pulse energy 1 mJ) for THG. The probe peak intensity was 2.9 GW/cm^2 (pulse energy 1.2 mJ). Green dots represent the experimental data. The blue line, along with the shaded area, indicates the mean and standard deviation of the data within wavelength bins of 20 pm. The dashed red line corresponds to a numerical simulation, offset by the mean background level (dotted black line). The dashed-dotted orange line (SFM only) marks the noise threshold, defined by the standard deviation of the background. For simplicity and faster calculation, we assumed a Lorentzian line shape instead of a Voigt profile. Markers indicate the central wavelengths of rovibrational two-photon resonances ($v = 0 \rightarrow 2$, Q-branch with $\Delta N = 0$ in the electronic ground state), with rotational quantum numbers N of the ground state for the transition (orange squares for $H^{35}Cl$, red diamonds for $H^{37}Cl$). Note that the logarithmic scale on the photon count axes limits the presentation of the background to positive values, though it contains negative values due to electronic noise as well.

3.3.2 SFM with Collinear Configuration

Initially, we experimented with SFM by aligning the probe beam collinearly with the fundamental beam through the gas cell. In this setup, the probe beam had a beam waist ($1/e^2$ radius) of 125 µm and a confocal parameter of 90 mm, which is closer to the fundamental beam's confocal parameter of 60 mm.

Fig. 3.9 presents the resulting SFM spectrum in HCl with this setup. Compared to the non-collinear case (see Fig. 3.8 (a)), the HCl pressure of 27 mbar and the fundamental peak intensity of 280 MW/cm^2 are similar. However, the probe peak intensity of 320 MW/cm^2 is an order of magnitude lower, due to the lower pulse energy of 630 µJ and the larger beam waist of 125 µm. Yet, the collinear case minimizes the wave vector mismatch Δk, which in turn increases the squared phase-matching integral $|J_3|^2$ by an order of magnitude [39]. Consequently, the maximum signal level is only half of the non-collinear case.

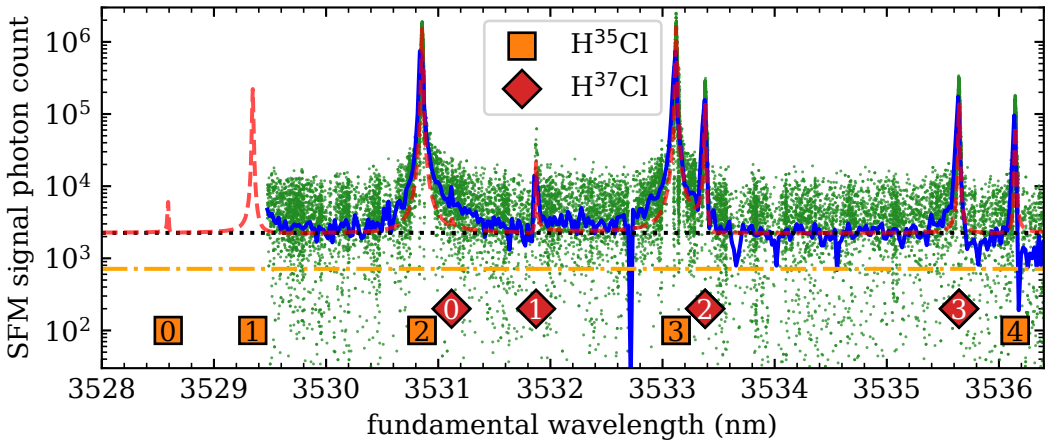

Figure 3.9: SFM signal photon count vs. fundamental wavelength for a collinear beam geometry. Green dots represent the experimental data. The blue line, along with the shaded area, indicates the mean and standard deviation of the data within wavelength bins of 20 pm. The dashed red line corresponds to a numerical simulation, offset by the mean background level (dotted black line). The dashed-dotted orange line marks the noise threshold of the non collinear setup. The HCl pressure was 27 mbar. The fundamental pulse energy was 920 µJ, while the probe pulse energy was 630 µJ (peak intensity 320 MW/cm^2). Note that the logarithmic photon count axis hides negative data points due to electronic noise.

The most notable difference between the spectra of the beam geometries is the increased background signal. The average background signal, reaching several thousand photons (dotted black line), surpasses the noise threshold observed in the non-collinear case (dashed-dotted orange line). This results in a tenfold increase in noise level and a corresponding reduction of the SNR to 300. Remarkably, the same background signal was observed even with an evacuated cell or when only a window was present in the beam path. This HCl-independent background signal stems from the cell windows and arises from a sum frequency process, as it is dependent on both the probe and the fundamental pulse energies. The non-collinear configuration effectively mitigates this issue; the 1° angle between the probe and fundamental beams ensures that their $1/e^2$ intensity spots are separated on the cell windows.

3.3.3 Energy Dependences

We analyze the energy dependence of the SFM signal and compare it to that of the THG signal and the theoretical expectation.

We measured the variation of the SFM signal pulse energy vs. fundamental and probe pulse energy (Figs. 3.10 (a) and (b)) at the strongest resonance of $H^{35}Cl$ at a fundamental wavelength of 3 533.12 nm (ground state $N = 3$). Exponential fits to the experimental data yield a power dependence with an exponent of 1.9(2) for the fundamental field (compared to an expected value of 2, see Eq. 1.1) and 0.9(1) for the probe field (compared to an expected value of 1). This confirms that the detected signal is indeed due to SFM.

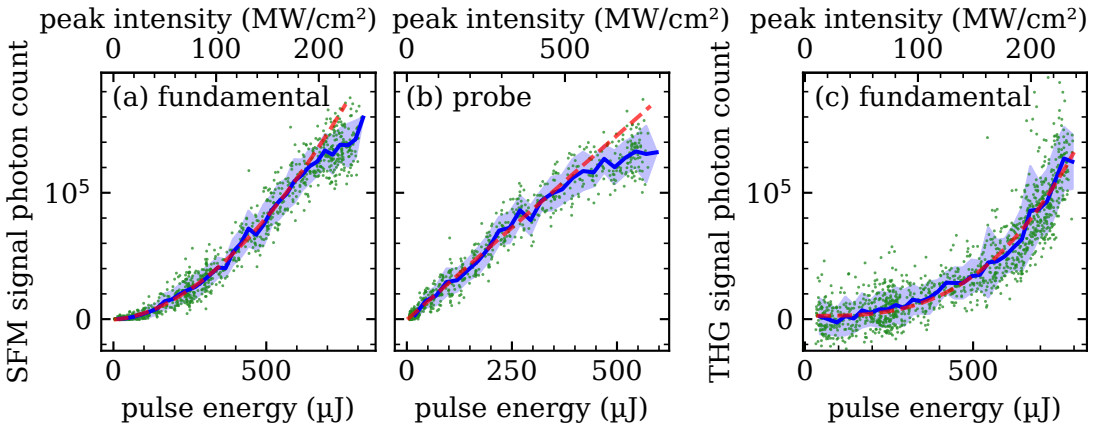

Figure 3.10: SFM signal photon count vs. (a) fundamental and (b) probe pulse energy (or peak intensity on the upper axis). The pulse energy of the other beam was kept at 500 µJ. Collinear beam geometry (probe beam waist of 175 µm). (c) THG signal photon count vs. fundamental pulse energy. The HCl pressure was 57 mbar for all measurements. Green dots show experimental data. The blue line and shaded area shows the pulse energy binned data and standard deviation. The dashed red line shows an exponential fit.

For comparison, Fig. 3.10 (c) shows the THG signal pulse energy as it varies with the fundamental pulse energy. An exponential fit to the experimental data yields an exponent of 2.9(6), which is close to the expected value of 3. In the center of the beam, we calculate the peak pulse area (product of two-photon Rabi frequency Ω and pulse duration τ) as $\Omega\tau \approx 8$. Averaging over the beam profile, we get an average pulse area well below unity. Thus, there are no saturation effects yet, as confirmed by our data. We assume that saturation of the PMT causes the SFM signal pulse energy to deviate from the exponential fit above a value of 120 000 photons.

3.3.4 Pressure Dependence and Particle Detection Limit

As the detection limit is an important feature for applications of nonlinear spectroscopy, we investigated the pressure dependence of the SFM signal.

For an accurate detection limit, precise pressure measurement is essential. The piezo sensor in our pressure sensor (VCR, Thyracont) provides reliable readings for pressures above a few mbar, particularly because its accuracy is independent of the

gas species. At lower pressures, the integrated Pirani sensor, which is better suited for low pressures, becomes active. However, the Pirani sensor is calibrated for N_2, and its readings vary with different gas species [40].

To calibrate the sensor, we filled the cell with 15 mbar of HCl, as measured by the piezo sensor, and repeated the procedure with N_2 for comparison. We then slowly evacuated the cell through a needle valve, maintaining the same valve position for both gases, while monitoring the Pirani sensor readings over time. By comparing the temporal evolution of the readings for both gases, and accounting for their different flow characteristics, we correlated the sensor reading for HCl with the factory-calibrated value for N_2. For more details see Ref. [39].

Fig. 3.11 (a) shows the number of SFM signal photons per pulse when we varied the HCl pressure. For maximal signal yield, we tuned the fundamental wavelength to the strongest two-photon resonance of $H^{35}Cl$ with $N(\nu = 0) = 3$ ($\lambda_f = 3\,533.12$ nm) and operated the laser system at a fundamental and probe pulse energy of 1.1 mJ. We performed two sets of measurements, either by a continuous variation of the pressure at fixed fundamental wavelength tuned to the expected two-photon resonance (see solid blue line in the figure), as well as by recording full spectral line profiles (see Fig. 3.11 (c)) at the transition for selected pressures. We fit Voigt profiles to the latter experimental data and indicate the maxima of the fitted profiles with cyan circles in Fig. 3.11 (a). This made sure that we observed the signal yield exactly at the resonance position, even if the latter varied slightly due to pressure-induced line shifts. We noticed a line shift up to 1 GHz at atmospheric pressure. Thus, pressure-induced resonance shifts play no role in the low-pressure range relevant for applications - as already a quick comparison of the two measurement sets in Fig. 3.11 (a) shows.

The pressure dependence yields an exponential growth for a signal level exceeding background noise. The exponent of 1.7(1) for SFM is very close to the predicted exponent of 1.85 from our numerical simulation. As expected from the simulation in Sec. 3.1.2, the signal yield grows with a slightly lower exponent than 2 for low pressures, reaches a maximum in an intermediate regime, and decreases for large pressures. We confirmed this behavior in SFM measurements towards larger pressures up to 700 mbar.

From the data we obtain a maximal SFM signal at a pressure around 30 mbar, while the signal decreases due to phase-matching issues at larger pressures. Our numerical simulation (the dashed red line in Fig. 3.11 (a)) confirms these findings. Buffer gas might affect the phase-matching integral.

For comparison, we also recorded the pressure dependence for THG with a fundamental pulse energy of 1 mJ. The situation is slightly different in THG spectroscopy (see in Fig. 3.11 (b)), where we observe an exponent of 1.6(1), while the simulation yields 1.86. However, this prediction depends a lot upon exact numbers for refractive indices, which are not known with sufficient precision.

From the data in Fig. 3.11 we determine a detection limit for THG and SFM, i.e., the minimal particle pressure which still permits observation of a spectral line. More accurately, we define the detection limit by the HCl pressure, at which the mean signal pulse energy exceeds the standard deviation of the background (see Fig. 3.11 (a) and 3.11 (b)). For SFM, the detection limit is 0.1 mbar (corresponding to 0.35×10^{15} $H^{35}Cl$ particles per cm^3 in the relevant ground state). As expected,

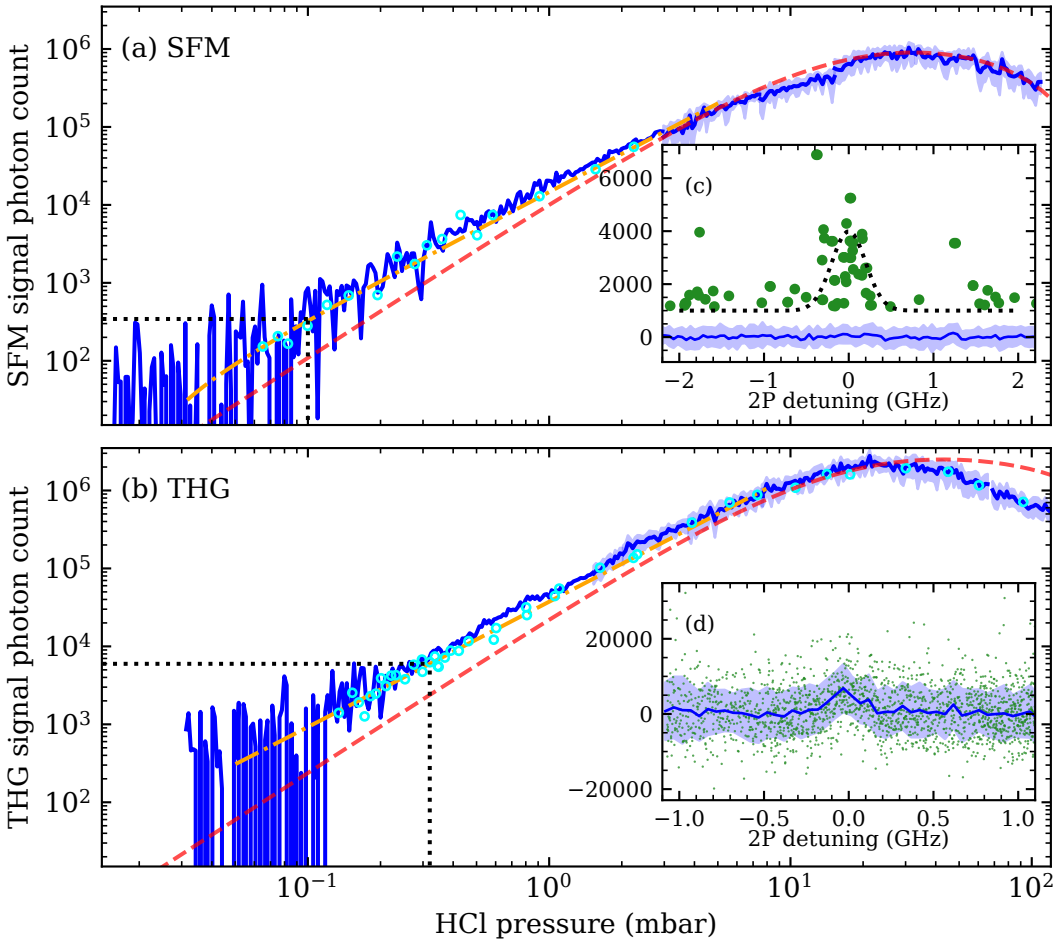

Figure 3.11: (a) SFM and (b) THG signal photon count per pulse vs. HCl pressure. The solid blue line represents experimental data from continuous variation of the HCl pressure at fixed fundamental wavelength (3 533.12 nm), binned in 0.01 logarithmic decade pressure intervals. The blue shaded area indicates the standard deviation. Cyan hollow circles show the maxima of Voigt fits to spectral lines at selected pressures. The dashed-dotted orange line is an exponential fit to the latter data, while the dashed red line corresponds to a numerical simulation. Dotted black lines mark the noise level and detection limit. Note the logarithmic scales on both axes. The insets show the spectral lines (photon count per pulse vs. two-photon (2P) detuning) at the detection limit, for (c) SFM at 0.1 mbar and for (d) THG at 0.32 mbar. The SFM background and the THG data is binned in 50 MHz intervals. For SFM, we distinguish between the electronic background in blue and the optical signal as green dots. The dotted black line is added to guide the eye.

this is well below 1.5 mbar, which we roughly estimated as an upper limit from the SFM spectrum. For THG, the detection limit is around 0.32 mbar (corresponding to 1.2×10^{15} particles per cm^3), which is an improvement compared to a previous work in our group on resonantly enhanced THG [37]. Nevertheless, SFM outperforms THG with regard to the detection limit. Even below the detection limit pressure defined by the above condition, we can identify spectral lines (see cyan data points below the detection limits in Fig. 3.11 (a,b), albeit with less confidence.

Figs. 3.11 (c) and 3.11 (d) show spectral lines at the detection limit for SFM and THG. For THG, the peak appears on top of large electronic noise, which is due to the need for amplification of the APD signal. This is a major and typical disadvantage of THG signal detection by an APD compared to the SFM scheme with a PMT. Also in the SFM measurement we find a constant baseline of electronic noise (see blue line) adding to optically generated signal (see green dots), which also contains optical background due to scattered radiation in the setup and ambient light. Nevertheless, the SFM peak at the detection limit is clearly visible.

The SNR could be improved by application of a PMT with larger quantum efficiency compared to 1 % of our device. Fig. 3.11 (c) shows, that this low quantum efficiency leads to only a few detected events (green dots) out of many single-shot measurements (1 000 per GHz) although there is a signal at the level of several photons. There are PMTs available with quantum efficiency towards 20 %. However, the devices were only available after our experiments.

Finally, we compare our result with the current workhorse CARS, as another nonlinear spectroscopic method. CARS is able to identify molecular species at pressures of 0.1 mbar [5]. Other applications of CARS determine, with a fs laser, concentrations of various molecules down to 1 % of a gas mixture [6]. Direct comparison is difficult, as the nonlinear susceptibility and thus the generated power differ greatly among various molecular species. Furthermore, many CARS implementations use ps or fs laser systems.

Nevertheless, the detection limit of 0.1 mbar for SFM is on a comparable level. Although we investigated pure HCl and foreign gas will increase the linewidth and decrease the signal level, our results show the potential of this approach.

3.3.5 THG and SFM Conversion Efficiencies

Finally we briefly discuss the signal photon yield and conversion efficiency in our THG and SFM experiments. From the data we roughly estimate the absolute value of the nonlinear susceptibility $\chi^{(3)}$ for THG as 56 pm^2/V^2 and for SFM as 42 pm^2/V^2 at a HCl pressure of 30 mbar. These values are less than our simulation results of 138 and 142 pm^2/V^2.

However, the phase-matching integral in the calculation for SFM assumes ideal conditions of perfectly collinear geometry, equal confocal parameters and focus position, and with equal pulse duration and vanishing delay for both fundamental and probe beams. An angle between the beams increases the phase mismatch, which reduces the phase-matching integral, as well as the effective interaction length [16]. Also, the two different confocal parameters reduce the phase-matching integral [41]. Therefore, we expect a lower signal for non-collinear (or non-perfect) SFM. The experimental data confirm this expectation: The photon count and the conversion

efficiency for THG are somewhat larger than for SFM (compare signals for large pressures in Fig. 3.11 (a) and 3.11 (b)). Nevertheless, even in this case the nonlinear susceptibility for SFM compensates for the losses due to the phase-matching integral and shorter effective interaction length, which in turn reduces the background noise efficiently. Thus, the obtained SNR is far better in SFM compared to THG. Even under the not optimal conditions for SFM, we achieved a lower detection limit compared to THG.

These results confirm our assumption, that the excited electronic state is relevant for THG. Without the excited electronic state, the numerical simulation predicts a lower value of only 11 pm^2/V^2.

By estimations we confirmed that many other molecules with relevance for applications, e.g., carbon dioxide (CO_2), have substantially larger nonlinear susceptibilities (see also Appendix A).

3.3.6 Summary of Results

We successfully implemented resonantly enhanced SFM as an alternative to THG spectroscopy. SFM demonstrated a significantly lower detection limit of 0.1 mbar, compared to 0.32 mbar for THG, which is already an improvement over the detection limit of 1 mbar in Ref. [8]. We also achieved a SNR that was more than an order of magnitude higher with 4 500 compared to 190. However, where THG requires a single beam, SFM is more complex. It needs additionally the probe beam, which has to intersect the fundamental beam in the focus and under a small angle to suppress background noise generated in the gas cell windows. This makes alignment more challenging, but the benefits of increased SNR and detection limit outweigh these challenges.

We also refined the accuracy of the THG simulation by including electronically excited states and a more accurate refractive index. As a result, the simulations align more closely with the experimental data, predicting that the number of photons generated by both THG and SFM are of the same order of magnitude. The superior performance of SFM is mostly due to the detector setup, despite its suboptimal configuration using a PMT with a low quantum efficiency. Switching to a PMT with a higher quantum efficiency would further enhance the SNR and improve detection capabilities.

Chapter 4

Frequency Up-Conversion of THG Signals by SFM

In this chapter we introduce the use of SFM for frequency up-conversion and show how we integrated it in our experimental setup. We also compare experimentally the detection of the mid-infrared THG signal, generated in HCl, by an APD with the detection of the up-converted signal of THG by a PMT. We are preparing a manuscript for publication about the main results.

4.1 Up-Conversion with SFM

Up-conversion typically uses SFM applying a strong pump field at frequency ω_p to convert a seed at ω_s (in our case the mid-infrared THG signal pulse) to a SFM signal at $\omega_{SFM} = \omega_p + \omega_s$ in a nonlinear crystal.

We will study now the conversion efficiency and its dependence upon the input pulse energies in more detail. We assume partial pump depletion, i.e, a weak incoming mid-infrared signal wave, which experiences depletion during the conversion process, and a strong pump wave, which is assumed to remain undepleted. From the simple text-book calculation of SFM for plane waves in partial pump depletion we find, that the number of generated SFM photons is simply proportional to the number of incoming THG photons [15]. Hence, the conversion efficiency (defined as the ratio of SFM photons vs. THG photons) does not depend upon the power of the THG wave, but only on the pump power as [15]

$$\eta = \sin\left(\beta\sqrt{P_p}\right)^2, \tag{4.1}$$

where β is a pre-factor involving the nonlinear susceptibility and length of the crystal, indices of refraction, and frequencies. This dependence of the conversion efficiency vs. pump power also remains (with some variation of the pre-factor β) when we assume Gaussian beams with identical confocal parameters and vanishing walk-off [12, 41]. We note that the oscillation of the conversion efficiency with pump power is due to back-conversion from the SFM wave to the THG wave by DFM with the pump wave, which becomes relevant when the SFM conversion efficiency approaches large values close to unity.

4.2 Experimental Setup for Frequency Up-Conversion

Between the experiments discussed in Ch. 3 and those presented in this chapter, we conducted tests using CO_2 as a test gas. Due to CO_2's different transition wavelengths, we significantly modified the laser system. Appendix A describes these

modifications together with preliminary experimental results. For the current experiments, we reconfigured the laser system entirely to generate light suitable for THG in HCl.

4.2.1 Laser System for Up-Conversion

The laser system for the experiments in this chapter contains most of the elements of the laser system described in Secs. 2.2–2.5, however, some elements changed. Also the alignment and beam parameters differ from the previous setup. This section focuses on the differences to the laser system described previously.

For these experiments, a second wavemeter (WS6-200, High Finesse) was introduced to directly measure the Aculight OPO's signal wavelength, while the first wavemeter (WS6-600, High Finesse) continued to measure the pump wavelength. By measuring with both devices simultaneously, we could continuously monitor the mid-infrared idler wavelength.

Compared to Sec. 2.4, the spatial filter for the pre-amplifier's pump radiation consists of two AR-coated N-BK7 lenses with 500 mm (LA1908-YAG, Thorlabs) and 50 mm (LA1131-B-ML, Thorlabs) focal lengths. This reduced focal length (50 mm instead of 60 mm) of the second lens results in a slightly reduced beam radius of 350 µm ($1/e^2$) at the place of the pre-amplifier's OPA crystal. The pump beam is collimated. An uncoated 100 mm focal length CaF_2 lens (LA5817, Thorlabs) focuses the mid-infrared idler beam into the OPA crystal for a smaller beam waist of 160 µm and a confocal parameter of 2 cm. With a pump pulse energy of 730 µJ, the idler pulses have a pulse energy of 12 µJ.

Compared to Sec. 2.5, the spatial filter for the power amplifier's pump radiation consists of two AR-coated N-BK7 lenses with larger focal lengths of 1 000 mm (LA1464-YAG, Thorlabs) and 750 mm (LA1978-YAG, Thorlabs). Also the pinhole differs, as it is a home-built steel pinhole with a 1 mm diameter hole. This leads to a larger beam radius of 1 mm horizontally and 1.4 mm vertically (walk-off-axis). An AR-coated CaF_2 lens (LA5817-E, Thorlabs) with a focal length of 100 mm collimates the pre-amplifier's idler radiation with a beam radius of 1.6 mm at the place of the power amplifier crystals. A new batch of dichroic mirrors (Laseroptik, CaF_2, HR-coated for 1 064 nm, HT-coated for mid-infrared wavelengths), with a higher damage threshold of 10 J/cm^2 (10 ns pulses at 1 064 nm), combines and separates the mid-infrared radiation with the pump radiation before and after the crystals, respectively. However, Furukawa *et al.* determined a damage threshold of 2.5 J/cm^2 (25 ns pulses at 1 053) for 5 % doped bulk LNB [42], while Bäder *et al.* successfully used such a crystal at a peak fluence of 2.7 J/cm^2 (8 ns pulses at 1 064 nm) [43]. Therefore, we limited the pump pulse energy to 80 mJ, corresponding to a peak fluence of 2.5 J/cm^2. This results in a mid-infrared pulse energy of up to 500 µJ. We monitor the energy of the mid-infrared pulses on an InAsSb photo detector (PD, P13243-011MA, Hamamatsu), calibrated by an energy meter (PE-10C, Ophir).

The Nd:YAG laser not only provides the pump radiation for the amplifier stages but also for the SFM process, as described in Sec. 2.3. To spatially filter the infrared radiation, a 500 µm diameter pinhole (HP-3/8-DISC-DIM-500, Lenox Laser) is placed between two AR-coated N-BK7 lenses with focal lengths of 1 000 mm (LA1464-YAG, Thorlabs) and 150 mm (LB1437-B, Thorlabs). The second lens focuses the beam to

a beam waist of 350 µm into a 12 mm long, AR-coated BBO crystal (SHG, A-Star), cut at angles $\theta = 22.9°$ and $\phi = 0°$ for type 1 SHG from 1 064 nm to 532 nm. A dichroic mirror (Laseroptik, HR-coated for 1 064 nm and HT-coated for 532 nm) reflects the infrared pump beam to a beam dump while transmitting the generated visible radiation, which then serves as the pump beam for the SFM process.

4.2.2 Gas Cell and Detection Setup

Fig. 4.1 illustrates the experimental setup for the up-conversion experiments. Tunable mid-infrared pulses at a wavelength of 3 533 nm serve as the fundamental radiation to drive resonantly enhanced THG via rovibrational states in HCl. A 150 mm focal length, AR-coated CaF_2 lens (L_1, LA5012-E, Thorlabs) focuses the beam into an 18 cm long gas cell, which is fitted with uncoated, wedged CaF_2 windows (WW51050, Thorlabs). The gas mixing panel, gas samples, and pressure sensor are those of the previous chapter, see Sec. 3.2.

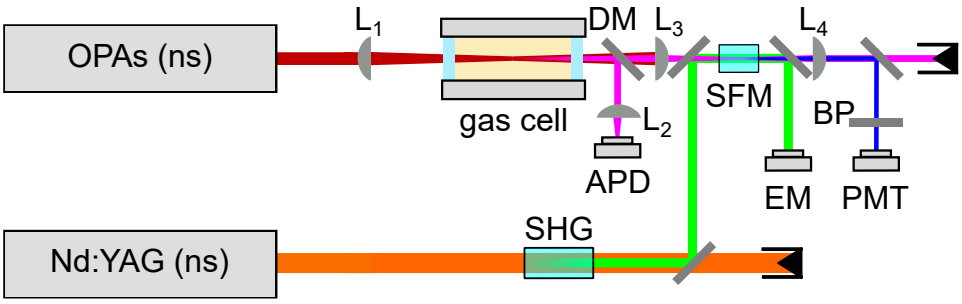

Figure 4.1: Experimental setup for the THG detection via SFM with the second harmonic (SHG) of the Nd:YAG laser, lenses (L), dichroic mirror (DM), avalanche photodiode (APD), energy meter (EM), bandpass filter (BP), and photomultiplier tube (PMT).

Fig. 4.2 shows the evolution of the fundamental beam radius as it propagates through the gas cell. The beam focus is 6 cm beyond the entry window and, therefore, slightly ahead of the cell's center. The beam waist ($1/e^2$ radius) of 220 µm with a confocal parameter of 9 cm results in a peak intensity around 100 MW/cm^2 for typical pulse energies used in the experiment.

To detect the weak THG signal generated at 1 178 nm in HCl, we separate it from the fundamental radiation using a series of optical elements: a dichroic mirror (DM, Laseroptik, HR-coated for near-infrared and HT-coated for mid-infrared wavelengths), a 5 mm thick AR-coated N-BK7 window (WG11050-C, Thorlabs) to block mid-infrared light, and a spectral edgepass filter (FELH1100, Thorlabs). The THG signal at 1 178 nm is then collimated and focused onto the 200 µm diameter active area of an APD (IAG-200-S6, Lasercomponents) using two AR-coated glass lenses (L_2) with focal lengths of 250 mm (LA4158, Thorlabs) and 100 mm (LA1509-C-ML, Thorlabs). The APD is equipped with a transimpedance amplifier (DLPCA-200, Femto) and was calibrated using weak pulses at 1 064 nm from the Nd:YAG laser.

To investigate frequency up-conversion of the THG signal, we simply remove the dichroic mirror DM (see Fig. 4.1) from the beamline. A lens system (L_3) with two uncoated CaF_2 lenses of focal lengths 100 mm (LA5817, Thorlabs) and 250 mm (LA5255,

Thorlabs) focus the THG wave into an uncoated BBO crystal (SFM, Castech) with a length of 12 mm and cut angles $\theta = 30°$ and $\phi = 0°$. From the measured beam waist ($1/e^2$ radius) of 190 µm for the fundamental beam, we estimated a beam waist of 110 µm for the THG signal beam in the crystal.

A half wave plate (lambda/2 532nm low, B. Halle) rotates the polarization of the 532 nm pump beam to parallel polarization with the THG beam, and an UVFS polarizing beamsplitting cube (435-1121, Eksma Optics) removes residual orthogonal polarization. An AR-coated N-BK7 lens system (not shown in Fig. 4.1) collimates this pump beam to an $1/e^2$ radius of 770 µm in walk-off-direction and 325 µm in the perpendicular direction, measured at the position of the SFM crystal. We typically use pulse energies up to a few mJ at 532 nm.

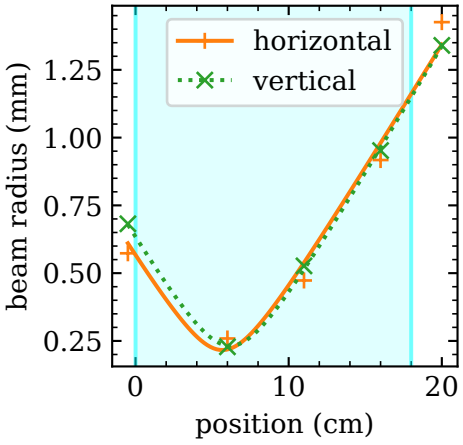

Figure 4.2: Beam radius ($1/e^2$) of the fundamental beam vs. position relative to the cell's entry window. The cyan shaded area indicates the position of the gas cell. Plus and cross markers indicate measurement data, while a solid and dashed line indicate a Gaussian beam fit for the horizontal and vertical beam radii, respectively.

We use a dichroic mirror (L-07228, Laseroptik) to combine the THG signal and the pump beams, that they interact in the SFM stage. The SFM type-I process up-converts the THG signal from 1 178 nm to 366 nm with orthogonal polarization. In the following we will call the up-converted radiation the "SFM signal", in contrast to the "THG signal" before up-conversion. A dichroic mirror (L-07228, Laseroptik), a longpass mirror (DMLP490, Thorlabs) and two bandpass filters (BP, FBH370-10, Thorlabs) serve to spectrally separate the SFM signal from pump radiation at 532 nm and optical background. An AR-coated N-BK7 lens (L_4, LA1509-A, Thorlabs) of focal length 100 mm collimates the divergent SFM signal beam onto a PMT (R14657, Hamamatsu). A digital oscilloscope (Picoscope 6426E, Pico Tech) with a bandwidth of 1 GHz and sample time of 0.2 ns samples the electric PMT signal. We calibrated the PMT with weak pump pulses at 532 nm, taking the small variation of the quantum efficiency of the PMT with 33 % at the SFM signal wavelength and 25 % at the pump wavelength into account.

4.3 Experimental Comparison of Frequency Up-Conversion of THG Signals by SFM

4.3.1 Preliminary Up-Conversion Test

First, we investigated the necessary pump pulse energy and achievable up-conversion efficiency, that is the ratio of seed photons up-converted via SFM [44]. For simplicity, we employed CW radiation instead of the THG signal as the up-conversion seed

beam.

Fig. 4.3 shows the modified experimental setup for these tests. A home-built OPO (see Appendix A) provided the seed radiation for the up-conversion process at 1 412 nm. It was chosen due to its proximity to a THG wavelength of CO_2 at 1 439 nm, which was the original target for up-conversion. A single-mode fiber transfers the seed to the up-conversion setup, and a polarizer (P) is used to correct for any polarization rotation caused by fiber bending. A lens system (L_1,) focuses the seed beam into the SFM crystal, producing a beam waist of 150 µm ($1/e^2$ radius). In this configuration, the pump beam has a beam radius of 400 µm inside the SFM crystal. Neutral density filters in front of the PMT attenuate the signal pulse energy as needed.

In a first test, we measured the generated SFM signal photon count for various seed photon counts by using neutral density filters (NENIR series, Thorlabs) to attenuate the seed beam. Fig. 4.4 (a) shows that, as expected, the signal photon count rises linearly with the seed photon count. We defined the seed photon count as the number of seed photons entering the SFM crystal during 6 ns, which is the FWHM duration of the pump pulse. A linear fit yields a conversion rate of 35 % of the seed photons.

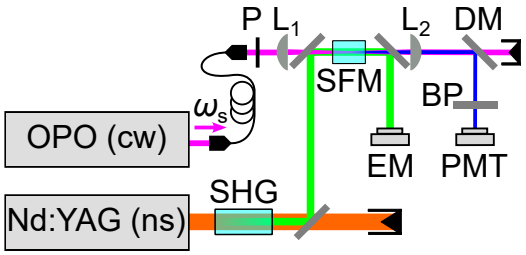

Figure 4.3: Experimental setup for the preliminary up-conversion tests with a CW OPO, polarizer (P), lensen (L), nonlinear crystals (SHG, SFM), dichroic mirror (DM), bandpass filter (BP), energy meter (EM), and photomultiplier tube (PMT).

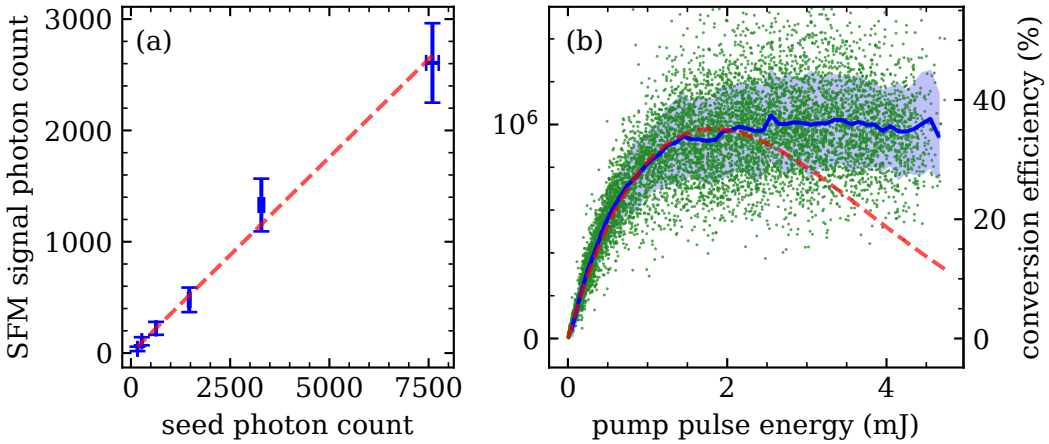

Figure 4.4: SFM signal photon count vs. (a) seed photon count and (b) pump pulse energy. The blue markers and error bars in the seed dependence indicate the mean value and standard deviation for a single measurement. In (b), green dots represents data points, while the blue line and shaded area indicates the mean value and standard deviation. The dashed red line indicates fits, linear for (a) and Eq. 4.1 for (b). For the seed dependence, the pump pulse energy was 1.8 mJ and for the pump pulse energy dependence, the seed power was 65 µW.

Fig. 4.4 (b) presents the signal photon count and conversion efficiency for various pump pulse energies, with an unattenuated seed power of 65 µW entering the SFM crystal. To account for the large signal pulse energy, larger than in the previous

measurement, neutral density filters were placed in front of the PMT for attenuation.

For pump pulse energies up to 0.5 mJ, the signal photon count increases almost linearly. As expected from Eq. 4.1, the growth rate of the signal photon count slows for larger pump pulse energies. Above 2.5 mJ, the signal photon count plateaus, contrary to Eq. 4.1, which predicts back-conversion of the signal energy to the pump and seed beams. However, the theory assumes vanishing walk-off, while the signal beam experiences 66 mrad walk-off, such that the generated signal radiation exits the interaction region, which prevents back-conversion. The conversion efficiency reaches a peak of 35 %, which is lower than the expected value of unity. We will explore the potential causes and possible solutions in detail, after presenting the up-conversion of the THG signal.

4.3.2 THG and Up-Conversion Spectra

Fig. 4.5 shows the SFM and THG signal spectra, when we tune the fundamental mid-infrared radiation close to two-photon resonances in HCl.

We compare the measured spectra with a numerical simulation, which fits well, both for frequency positions as well as relative line strengths. The SNR, i.e., the ratio between the maxima and the standard deviation of the background, is 450 for the SFM spectrum and 17 for the THG spectrum. Thus, up-conversion of the THG signal improves the SNR significantly, due to much larger amplification and lower noise in the PMT compared to the APD with additional amplifier. As a consequence, the SFM spectrum reveals several resonances at lower signal yield, which in the THG spectrum vanish in the background. From the THG and SFM photon counts at the most intense resonance in our scan range at 3 533.12 nm (ground state $N = 3$ in $H^{35}Cl$, see also Fig. 3.1) we calculated an up-conversion efficiency of 12 % with respect to the signal photon numbers. A detailed discussion of the conversion efficiency, including contributing factors and possible solutions, will follow in the next section. Nevertheless, the results showed that a good amount of mid-infrared THG signal photons are converted to the shorter SFM signal wavelength of 366 nm. This underscores the advantage of detection by a PMT, whose greater amplification compensates for photon losses in the up-conversion stage.

4.3.3 Up-Conversion Energy Dependence

Fig. 4.6 shows the measured dependences of the generated SFM (up-conversion) signal with the incoming THG and pump waves in our experiment. Let us first consider the variation with the THG pulse energy, while keeping the pump pulse energy fixed.

As in our setup we cannot detect the THG signal and the SFM signal simultaneously, we measured the dependence upon the third power of the fundamental pulse energy instead, which is proportional to the generated THG pulse energy according to $E_{\mathrm{THG}} \propto E_{\mathrm{f}}^3$. Fig. 4.6 (a) shows the SFM signal photon count vs. the cubic power of the fundamental pulse energy. The dependence is, as expected, linear in the THG pulse energy or in the third power of the driving fundamental pulse energy.

To calculate the conversion efficiency, we needed to determine the number of THG photons generated. To achieve this, we directly measured the THG signal using the

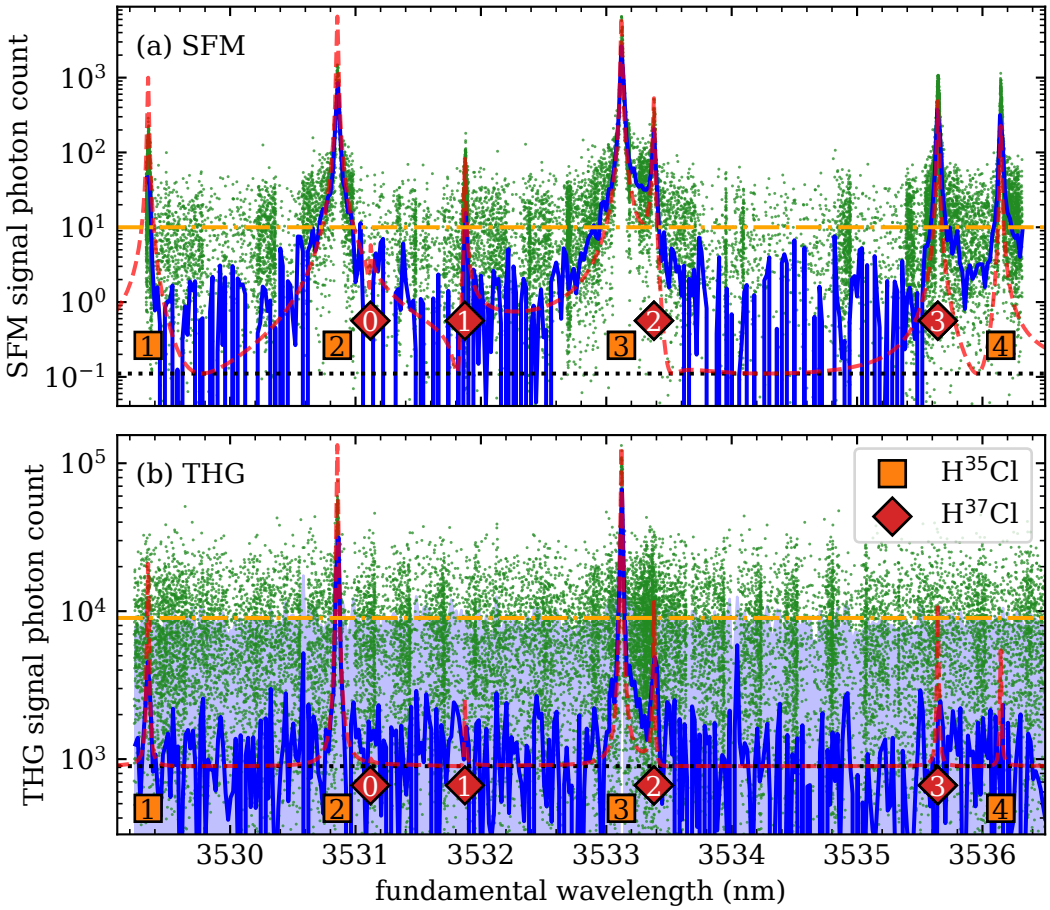

Figure 4.5: (a) SFM signal and (b) THG signal photon counts vs. fundamental wavelength. Green dots show experimental data, the blue line and blue shaded area show the mean value and standard deviation of wavelength binned data. The dashed red line shows a simulation, normalized to the maximum of the experimental data and offset by the mean background (indicated by the dotted black line). The background is mainly due to electronic noise. The dashed-dotted orange line shows the noise level (standard deviation envelope of the background signal). Markers indicate the central wavelengths of rovibrational two-photon resonances ($\nu = 0 \rightarrow 2$, Q-branch with $\Delta N = 0$ in the electronic ground state), with rotational quantum numbers N of the ground state for the transition (orange squares for $H^{35}Cl$, red diamonds for $H^{37}Cl$). The HCl pressure is 29 mbar, the fundamental pulse energy is 350 µJ, for SFM the pump pulse energy is 2.3 mJ. Note the logarithmic scale on the vertical axis for the photon counts. Electronic noise at negative values is hidden in this logarithmic representation. The photon counts refer to the number of signal photons which reached the detectors, after losses at optical components. Note that the scan method (see Sec. 3.3.1) combines different independent modulation techniques, which leads to the repeating accumulation and scarcity of data points in the spectrum between simulation peaks.

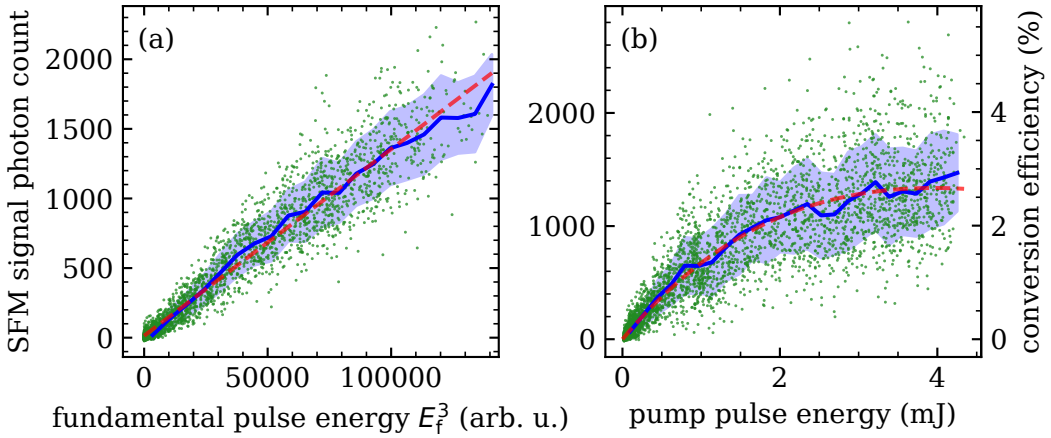

Figure 4.6: SFM signal photon count vs. (a) fundamental pulse energy E_f^3 and (b) pump pulse energy. Green dots represent experimental data. The solid blue line shows the mean value and the shaded area the standard deviation of the intensity-binned data. The dashed red line show fits to the data, a linear function in (a) and Eq. 4.1 in (b). The HCl pressure in the experiment was 29 mbar and the wavelength of the fundamental wave was set to the strongest line in the THG spectrum at 3 533.12 nm. For the dependence upon the THG pulse energy, the pump pulse energy was set to 3.7 mJ. For the dependence upon the pump energy, the pulse energy of the fundamental mid-infrared wave was set to 400 µJ. Note that the photon count refers to the number of signal photons which reached the detectors, while the SFM conversion efficiency is defined with regard to the number of SFM signal photons generated in the up-conversion crystal, taking transmission losses in the optical beamline into account.

APD at various fundamental pulse energies. This allowed us to establish a relationship between the number of generated THG photons and the fundamental pulse energy. A linear fit to the data revealed a ratio of 1.35 % between detected SFM photons and detected THG photons (based on this calibration). After accounting for the different transmission efficiencies of the THG and SFM signal beam lines, this corresponds to a conversion efficiency of 2.4 %. This is less than the 12 % conversion efficiency we achieved during the recording of the spectra. It is even less than the 35 % we reached in our preliminary tests with some attenuated CW mid-infrared radiation instead of the low-power THG signal beam.

The better efficiency in the preliminary tests is due to the fact, that the beam path for the mid-infrared CW laser beam at macroscopic power level was easy to match with the pump beam in the SFM crystal. In contrast, for the weak THG signal we could only approximate the focus position and beam width during alignment, let alone focus it in a way that would match its confocal parameter to that of the pump beam or the crystal length. Ref. [41] shows that the conversion efficiency decreases by several orders of magnitude if the confocal parameters of the interacting waves and the crystal length are not optimally matched. Additionally, the 70 mrad walk-off of the SFM signal beam across the 12 mm crystal length further reduces the efficiency by almost an order of magnitude. Thus, the reduced conversion efficiency can be attributed both to the mismatch between the confocal parameters of the laser beams themselves and their mismatch with the crystal length, as well as to the beam walk-off within the crystal.

Let us now look how the conversion efficiency depends on the driving pump pulse energy. Fig. 4.6 (b) shows the conversion efficiency, that is the measured variation of the SFM signal photon count for a fixed fundamental pulse energy, vs. the driving pump pulse energy. For pump pulse energies below 1 mJ, the number of SFM photons (and, hence, the conversion efficiency) increases approximately linearly, as expected from simple theory. For larger pump pulse energies, the slope of the dependence decreases as the THG signal gets more depleted, and becomes negative for pump pulse energies above 4 mJ. This follows the dynamic described by Eq. 4.1, albeit with a maximum conversion efficiency (with regard to the signal photon numbers) of only 2.4 %. In the preliminary tests, the conversion efficiency also followed the same sinusoidal form until it reached the peak, then it leveled off into a plateau. This suggests that it is not possible to increase the conversion efficiency by increasing the pump pulse energy.

4.3.4 Particle Detection Limit and Pressure Dependence

We turn now our attention to the particle detection limit. As the comparison of the SFM and THG spectra above (see Fig. 4.5) already showed, the signal yield and SNR is much larger, when we apply the SFM up-conversion stage. Obviously, this will also improve the detection limit, i.e., the smallest amount of molecules, which is observable with sufficient signal yield above the noise level. Hence, the detection limit is the most important property to evaluate the performance of our SFM up-conversion approach for applications in spectrometry. Therefore, we measured the SFM and THG signal while varying the HCl pressure in the gas cell.

Figs. 4.7 (a,b) show that the signal photon count increases exponentially for larger pressures for both the SFM and THG signal. An exponential fit to the SFM data yields an exponent of 1.3, while for the THG data the exponent is 1.5, which is slightly less than the 1.85 expected from theory, see Sec. 3.1.2, but confirms our experimental findings in Sec. 3.3.4. At a HCl pressure of 0.7 mbar, the SFM signal is equal to the background noise level (i.e., the envelope of its standard deviation, see dotted black line in Fig. 4.7 (a)), which we define as the detection limit. At this pressure we have 2.5×10^{15} particles per cm^3 in the relevant rovibrational ground state of $H^{35}Cl$. We note that there is still SFM signal observable even at lower pressure, below our conservative definition of the detection limit. When we compare the SFM data to the THG signal, we find that THG reaches the detection limit already at 8.5 mbar (see Fig. 4.7(b)).

These data demonstrate a significant improvement of the detection limit by the SFM up-conversion stage, which enables application of a sensitive PMT detector with large gain and low noise to detect photons at shorter wavelength — compared to detection of mid-infrared THG photons by an APD. This is the case, even though the additional SFM up-conversion process reduces the number of signal photons for detection.

Note that the low resolution of the piezo pressure sensor (0.1 mbar) results in the visible discrete pressure steps between 4 mbar and 9 mbar in Fig. 4.7. At lower pressures, the sensor switches to its higher-resolution Pirani mode.

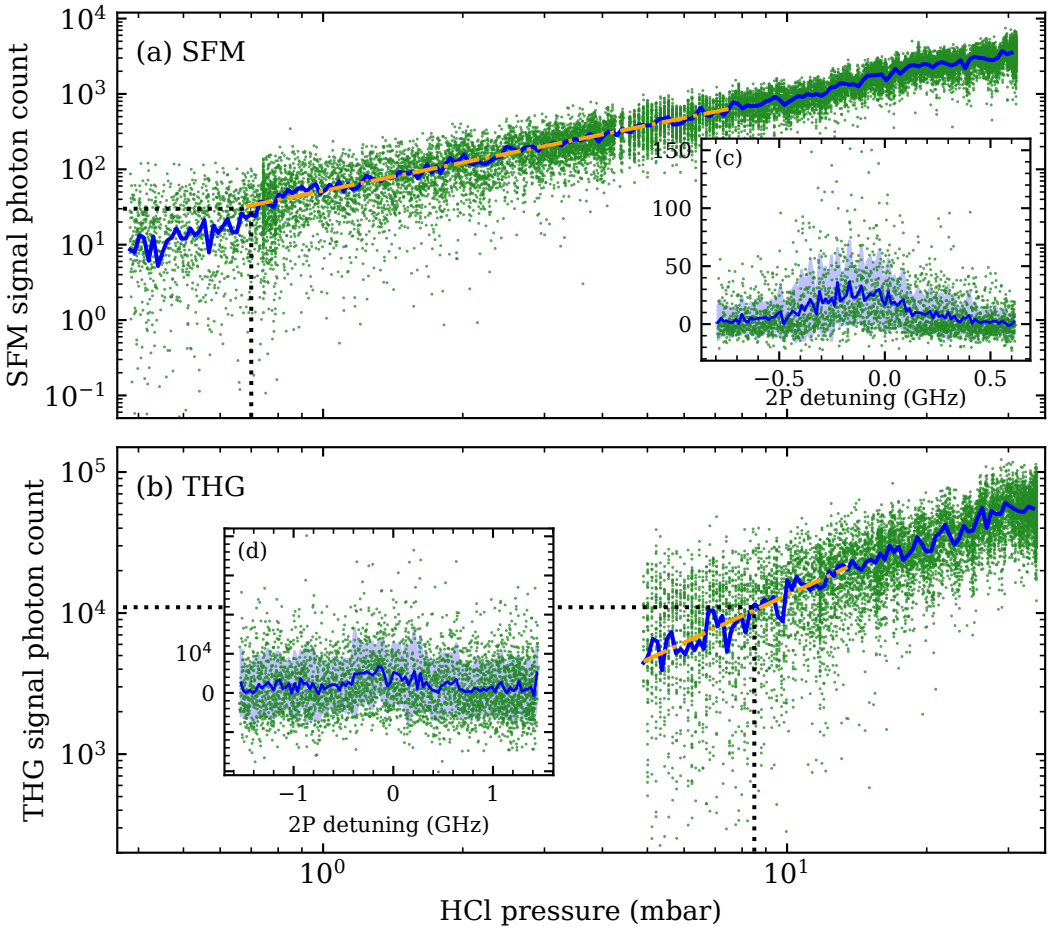

Figure 4.7: (a) SFM and (b) THG signal photon counts vs. HCl pressure. Green dots represent experimental data. The solid blue line and shaded area represent the mean value and standard deviation of the intensity binned data. The dashed-dotted orange lines indicate an exponential fit to the measurement data. The dotted black lines indicate the detection limit, defined by the standard deviation envelope of the background noise. The wavelength of the fundamental wave was set to the strongest line in the THG spectrum at 3 533.12 nm. The fundamental pulse energy was 330 µJ and for SFM the pump pulse energy was 2 mJ. Note the logarithmic scale on both axes. The insets show the (c) SFM and (d) THG signal photon count vs. two-photon detuning from the resonance at 3 533.12 nm at a HCl pressure of 0.8 and 5 mbar, respectively. Green dots represent experimental data and the blue line and shaded area represent the mean value and standard deviation of the frequency binned data.

4.3.5 Technical Considerations

Finally, we must not fail to mention the technical issues associated with the setup involving the SFM up-conversion stage. Of course, the additional SFM stage means an extension of the detection beamline by a few extra optical elements (with the nonlinear optical crystal as the main component) and alignment of the phase-matching angle, as well as the overlap between the mid-infrared THG signal and the pump beam at 532 nm.

Due to the rather large diameter of the pump beam, as well as the larger sensitivity of the PMT detector for the SFM signal at shorter wavelengths, alignment of the pump and THG beam is no problem at all. Moreover, the few extra bits of technical equipment and moderate extra efforts for alignment of the up-conversion stage are more than compensated for by the technical benefit of a much larger active area of the PMT compared to the APD. This makes alignment of the signal onto the detector much simpler — which we found very convenient in the up-conversion setup.

4.3.6 Summary of Results

We successfully employed SFM to up-convert the signal radiation from resonantly enhanced THG in HCl into the visible spectrum, enabling detection via a PMT as an alternative to direct APD-based detection.

Achieving a conversion efficiency of 12 % in terms of the number of converted photons, we enhanced the SNR of the THG spectrum 26-fold, from 17 to 450. This improvement reduced the detection limit from 8.5 mbar in the APD-based setup to 0.7 mbar in the up-conversion setup. Additionally, we examined the input energy dependence of the SFM up-conversion process, confirming a linear relationship with the THG signal pulse energy and a sinusoidal dependence on the pump pulse energy.

We note that the larger SNR, lower detection limit, and technical benefits of the additional SFM up-conversion stage are also an advantage compared to other variants of THG spectroscopy like resonantly enhanced SFM inside the medium itself (see Ch. 3).

Conclusion and Outlook

The research project dealt with the detection of molecules using resonantly enhanced sum frequency mixing (SFM) at rovibrational resonances with mid-infrared transition frequencies. Such resonances cause characteristic molecular spectra, making it possible to identify the molecules. Using mid-infrared radiation close to rovibrational transitions offers a large nonlinear susceptibility as multiple transitions have simultaneously small detunings, enhancing the overall detection sensitivity.

Previously, our group successfully implemented resonantly enhanced third harmonic generation (THG) for hydrogen chloride (HCl) detection, achieving a detection limit of 1 mbar [8]. In this work, we explored both SFM within the medium itself and up-conversion of the THG signal via SFM to improve the signal-to-noise ratio (SNR) and detection limit of spectroscopic measurements. While sensitive detection of the mid-infrared THG signal is challenging, the use of photomultiplier tubes (PMTs), which offer high gain in the visible range, promises more sensitive detection.

We successfully implemented resonantly enhanced SFM of intense narrowband mid-infrared laser pulses and near-infrared laser pulses in HCl with a PMT based detection setup as an alternative to THG spectroscopy. Similarly to THG, SFM of mid-infrared laser pulses is close to one- and two-photon resonances with detunings typically in the range of a few hundred GHz. Our experimental comparison demonstrated that SFM outperforms THG in terms of sensitivity, offering a lower detection limit of 0.1 mbar, compared to 0.32 mbar, and a significantly higher SNR of 4 500, compared to 190. Although SFM requires more complex alignment due to the additional beam, its performance outweighs this challenge, making it a promising method for future applications.

Furthermore, we improved the numerical simulations for THG by incorporating electronically excited states and a more accurate refractive index calculation. These improvements resulted in a better alignment between the simulated and experimental data. The simulations reveal that both THG and SFM signals exhibit a pressure dependence slightly below the quadratic relationship, with an exponent of 1.85 due to phase-matching effects. This aligns closely with our experimental findings, where we observed an exponent of 1.6 for THG and 1.7 for SFM. The simulations predict only a slightly larger number of generated photons for SFM, compared to THG. Therefore, we attribute the superior performance of SFM primarily to the detection setup. The higher internal gain of the PMT, compared to the avalanche photodiode (APD) used for THG, accounts for this advantage. Notably, a more efficient PMT could further enhance the SNR of SFM.

Besides using SFM inside the medium, we successfully up-converted up to 12 % of the THG signal photons into the visible spectrum using SFM in a nonlinear crystal. We found that up-conversion improves the detection limit from 8.5 mbar, for direct detection of the THG signal, to 0.7 mbar, and it increases the SNR by a factor of 26. While this up-conversion setup requires an additional SFM stage and, in our case, a second harmonic generation (SHG) stage to generate the pump wave, the alignment of the up-conversion setup was simpler compared to THG detection, which

was hindered by the small area of the APD.

Ultimately, both approaches — SFM in the medium itself and up-conversion of the THG signal — demonstrated an increased sensitivity by shifting the detection to the visible spectrum, where more sensitive detectors are available. This highlights the potential of these techniques to significantly improve molecular detection in the mid-infrared regime.

Outlook

We already started to apply resonantly enhanced THG spectroscopy and up-conversion to carbon dioxide (CO_2). However, the pulse energy of the laser system modified to generate light at the longer wavelength range around 4 300 nm was only 10 µJ due to the high mid-infrared absorption in the amplifier nonlinear medium, lithum niobate.

For systematic studies, we need an order of magnitude more pulse energy. Currently, we are working on a nanosecond optical parametric oscillator (OPO) to generate mJ mid-infrared pulses at 1 400 nm. These pulses will seed an optical parametric amplifier (OPA) in order to generate mJ mid-infrared idler pulses. These intense pulses will allow us to repeat our investigation with CO_2 as a test gas. Preliminary results, see Appendix A, already revealed a significant signal despite the low pulse energy due to the large nonlinear susceptibility of CO_2.

With CO_2, future research will investigate new applications of THG and SFM. The relative line strengths in a molecular spectrum depend on the temperature dependent state population. Due to CO_2's lower rotational constant, more ground states are occupied simultaneously, which allows a more precise temperature measurement. The first application will be implementing and evaluating temperature measurements via THG or SFM.

Another application is detection of CO_2 at higher temperatures and in mixture with foreign gas. Eventually, we will apply these nonlinear spectroscopy methods to a live flame, as a step towards applications like combustion analysis.

Zusammenfassung

In der vorliegenden Arbeit ging es um die Moleküldetektion mittels resonant überhöhter Summenfrequenzmischung (SFM) an Rovibrationsresonanzen mit mittelinfraroten Übergangsfrequenzen. Solche Resonanzen verursachen charakteristische Spektren, mit denen man die Moleküle identifizieren kann. Durch die Nutzung mittelinfraroter Strahlung nahe dieser Rovibrationsübergänge kann eine große nichtlineare Suszeptibilität erreicht werden, da mehrere Übergänge gleichzeitig nur wenig verstimmt sind, was die Detektionssensitivität erhöht.

Unsere Arbeitsgruppe hat zuvor die resonant überhöhte Erzeugung der dritten Harmonischen (THG) zur Detektion von Chlorwasserstoff (HCl) eingesetzt und damit eine Detektionsgrenze von 1 mbar erreicht. In dieser Arbeit wurde Summenfrequenzmischung im Medium selbst und die Frequenzkonversion des THG-Signals mittels SFM untersucht, um das Signal-zu-Rausch Verhältnis (SNR) und die Detektionsgrenze der Spektroskopiemessungen zu verbessern. Photomultiplier (PMTs) versprechen mit ihrer großen Verstärkung eine sensitivere Detektion, insbesondere im sichtbaren Spektralbereich, wohingegen es eine Herausforderung ist, mittelinfrarote Strahlung zu detektieren.

Resonant überhöhte SFM mittels intensiver, schmalbandiger, mittel-infraroter Laserpulse und nah-infraroter Laserpulse wurde erfolgreich umgesetzt. SFM mittelinfraroter Pulse ist, vergleichbar zu THG, gleichzeitig nah-resonant mit ein- und zwei-Photonen Resonanzen, wobei die Verstimmung typischerweise wenige hundert GHz beträgt. In den durchgeführten Experimenten schlägt SFM THG bezüglich Sensitivität, mit einer Detektionsgrenze von 0,1 mbar im Vergleich zu 0,32 mbar, außerdem ist das Signal-zu-Rausch Verhältnis von 4 500 deutlich höher im Vergleich zu 190. Auch wenn SFM aufgrund eines zusätzlich erforderlichen Laserstrahls höhere Anforderungen an die Justierung hat, so sind die erzielten Ergebnisse diese zusätzliche Mühe mehr als wert.

Außerdem wurde die numerische Simulation für THG verbessert, indem die elektronisch angeregten Zustände berücksichtigt werden und der Brechungsindex genauer berechnet wird. Diese Verbesserungen sorgen für eine größere Übereinstimmung zwischen simulierten und gemessenen Daten. Die Simulation zeigt, dass sowohl das THG- als auch das SFM-Signal eine Druckabhängigkeit haben, die nicht ganz quadratisch ist, sondern wegen Phasenanpassungseffekten einen Exponenten von 1,85 hat. Dies ist nahe an den experimentellen Ergebnissen mit einem Exponenten von 1,6 für THG und 1,7 für SFM. Die Simulationen sagen nur eine wenig größere Anzahl an SFM Photonen im Vergleich zu THG vorher. Das weißt darauf hin, dass die höhere Sensitivität bei SFM hauptsächlich vom Detektionsaufbau herrührt. Grund dafür ist die höhere interne Verstärkung des PMTs im Vergleich zur Avalanche-Photodiode (APD), die zur Detektion des THG-Signals verwendet wird. Ein effizienterer PMT könnte das SNR von SFM noch weiter steigern.

Neben SFM im Medium selbst wurden auch 12 % der THG Signalphotonen mittels SFM in einem nichtlinearen Kristall ins sichtbare Spektrum konvertiert. Im experimentellen Vergleich verbessert die Frequenzkonversion die Detektionsgrenze von 8,5 mbar, für die direkte Detektion von THG, zu 0,7 mbar. Auch verbessert sie das

SNR um einen Faktor von 26. Obwohl die Frequenzkonversion eine zusätzliche SFM Stufe und, in unserem Fall, eine Frequenzverdopplungsstufe für die Pumpwelle benötigt, war die Justage des Frequenzkonversionsaufbaus einfacher als für die THG Detektion, die durch die kleine Fläche der APD erschwert wurde.

Abschließend haben beide Ansätze, SFM im Medium selbst und Frequenzkonversion des THG-Signals, eine erhöhte Sensitivität gezeigt, indem sie die Detektion in das sichtbare Spektrum verschoben haben, wo es sensitivere Detektoren gibt. Dies zeigt das Potential der beiden Techniken, um die Molekülдetektion im mittel-infraroten Bereich zu verbessern.

Appendix A

THG and SFM Spectroscopy in Carbon Dioxide: Preliminary Results

We also investigated resonantly enhanced THG with carbon dioxide (CO_2) as a test gas. We preferred to work with CO_2, as it is unarguably one of the most relevant molecules [45] and its rovibrational transition dipole moments of 1×10^{-30} C m are an order of magnitude larger than those of HCl [19]. However, we faced serious challenges generating the necessary fundamental radiation at a wavelength of 4 260 nm such that we achieved only preliminary experimental results.

In this chapter, we present the modified laser system, featuring a custom-built OPO integrated to seed the OPA stages, along with the challenges encountered during its development and operation. Following that, we discuss the preliminary results achieved using this system.

A.1 Test Gas Carbon Dioxide

CO_2 is a small, linear, triatomic molecule, it is also stable and relevant, fulfilling our criteria for a test gas (see Sec. 2.1). Its most abundant isotope is $^{12}C^{16}O_2$, which constitutes 98.4 % of natural CO_2 [19].

The first excited electronic state $1^1\Pi_g$ exhibits a dipole-forbidden transition to the ground state $X^1\Sigma_g^+$ with a transition wavelength of 140 nm (corresponding to a wavenumber of 71 299 cm^{-1}). However, the next accessible state is $1^1\Sigma_u^+$, which is more relevant for THG, as it has a dipole-allowed transition at 112 nm (89 044 cm^{-1}) with a transition dipole moment of 5.44×10^{-30} C m [46].

CO_2 has three vibrational modes: symmetric stretching (wavenumber 1 333 cm^{-1}), asymmetric stretching (2 349 cm^{-1}), and bending (667 cm^{-1}). Only the asymmetric stretching and bending modes are infrared-active due to non-zero transition dipole moments between vibrational states [47]. The asymmetric stretching mode has the shortest transition wavelength of 4 260 nm and a transition dipole moment of 1×10^{-30} C m. For the third overtone, relevant for THG, the transition dipole moment is 0.002×10^{-30} C m [19].

A.2 Laser System for Carbon Dioxide

The laser system used for HCl (see Secs. 2.2–2.5) is limited to wavelengths below 3 900 nm due to the Aculight OPO, rendering the setup unsuitable for CO_2 with a transition wavelength around 4 260 nm. The pre-amplifier's PPLN crystal, however, offers poling periods suitable for phase-matching at these wavelengths. Also the power amplifier's bulk LNB crystals are suitable as they require a manageable 5° tilt for phase-matching.

Therefore, we designed and built an OPO to generate tunable mid-infrared radiation around the transition frequencies at 4 260 nm. The design is similar to the Aculight OPO: a fiber pump laser (YAR-15K, IPG Photonics) provides up to 15 W pump power at a wavelength of 1 064 nm for an OPO process in a PPLN crystal. The crystal is placed in a bow-tie cavity with two curved mirrors (50 mm radius of curvature) and two planar mirrors, all of which are HR-coated for the signal beam and HT-coated for the pump and idler beams.

An intra-cavity etalon, consisting of an uncoated 0.8 mm thick YAG plate (No. 101562, Layertec), keeps the signal radiation in a single longitudinal mode. However, due to temperature-induced fluctuations in the cavity length, the signal wavelength tends to drift during operation. To counteract this, we implemented a temperature stabilization system using pulse-width modulated heating, controlled by a PID system, managed via an Arduino [48]. The 50 mm long, 1 mm wide PPLN crystal (HC Photonics) has poling periods from 27 to 29 µm in a fanout structure across its 12 mm height. It is AR-coated for an OPO process involving a pump at 1 064 nm wavelength and an idler in the wavelength range 3 900–4 500 nm. A heatable oven (TC038D, HC Photonics) maintains a constant crystal temperature from room temperature up to 200°C. Ref. [49] describes the OPO and contains the design files.

Across a wavelength range of 3 900 to 4 500 nm, the OPO outputs up to 100 mW, measured by a power meter (3A, Ophir) [26, 50]. This is an order of magnitude less than the Aculight's output power of more than 1 W due to high idler absorption in the PPLN crystal.

We also determined the transmission of the amplifier material, MgO doped LNB. The OPO's idler radiation passes two uncoated, 0.5° wedged CaF_2 windows (WW51050, Thorlabs), which reflect a small fraction onto two calibrated InAsSb photodiodes (P13243-011MA, Hamamatsu). We recorded two transmission spectra, one with an AR-coated 3 cm long bulk LNB crystal (taken from the power amplifier, see Sec. 2.5) and one with N_2 between the windows, by changing the poling period of the OPO's PPLN crystal via vertical translation [48]. Fig. A.1 shows that LNB transmission decreases from 65 % at 3 950 nm to 10 % at 4 500 nm with a small plateau of 20 % between 4 200 and 4 350 nm, where also CO_2 resonances are. The transmission follows the same shape as determined by Ref. [30] (dashed red line, scaled according to Beer's law to 3 cm), but is lower as we include surface reflectivity, which Lin *et al.* do not include.

Additionally, water, which is present in the lab air, has absorption lines in the wavelength range of the OPO's signal radiation at 1 412 nm. As the cavity is resonant for the signal radiation, the water absorption has a large influence: stronger resonances inhibit the OPO process altogether and weaker resonances make the signal radiation hop continuously between different longitudinal modes.

Finally, we observed that during a 100 GHz scan of the pump wavelength, covering half of the tuning range, while maintaining a constant signal wavelength, the idler beam profile shifted gradually from a TEM_{00} Gaussian mode to a donut mode [26]. This behavior is consistent with the findings of Ref. [51], which demonstrated that the relative power distribution among transverse modes depends on the wave vector mismatch Δk. By adjusting the crystal's poling period, the wave vector mismatch can be tuned for a given set of wavelengths (pump, signal, and idler), thereby modifying

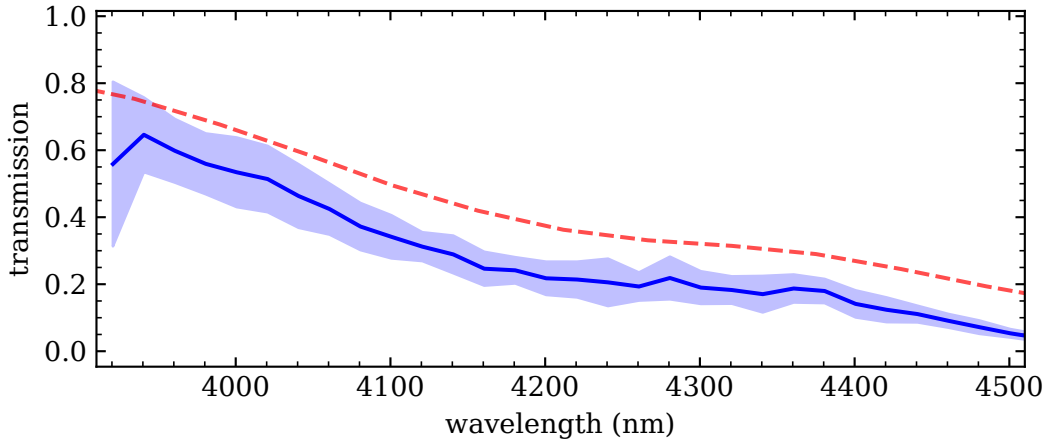

Figure A.1: Transmission vs. wavelength for an AR-coated 3 cm long 5 % MgO doped LNB. The blue line represents the data binned in 20 nm intervals, while the shaded area indicates the standard deviation. The dashed red line indicates literature values [30].

the beam profile. This allows for the generation of mid-infrared light at any idler wavelength in a TEM_{00} mode, suitable for seeding the OPA chain.

LNB's significant absorption of the mid-infrared radiation also introduces an amplification threshold, E_{amp}, which represents the pump pulse energy at which the amplification of the mid-infrared pulses surpasses the losses due to absorption. For the pre-amplifier, this threshold is 450 µJ, which is close to the damage threshold, leaving little margin for increasing the pump pulse energy beyond the amplification threshold. Consequently, even small fluctuations in the pump pulse energy E_p can cause substantial relative variations in the portion of the energy above the threshold, $E_p - E_{amp}$. This, in turn, leads to large fluctuations in the mid-infrared pulse energy, with the standard deviation sometimes reaching up to 100 % of the mean pulse energy.

The two-photon and three-photon resonances are close (a few GHz) to single photon resonances, such that ordinary air, which contains around 450 ppm CO_2, absorbs a substantial amount of the pulse energy. Therefore, we placed the whole OPO/OPA chain up to the gas cell's entry window in closed boxes and purged these with N_2. This also reduced the air humidity in the OPO, solving the issue of water absorption lines. The absorption of LNB, the material of the OPA crystals, remains high, however, such that the pulse energy, generated by pre-amplifier and power amplifier, was only around 10 µJ in the gas cell [26].

A.3 Experimental Setup

We used our numerical simulation (see Sec. 3.1), adapted for CO_2 and the modified laser system, to design the setup and to choose the most promising wavelength and pressure for ease of alignment.

At room temperature, the simulation predicts the largest THG signal for the excitation path $|N = 24\rangle \rightarrow |23\rangle \rightarrow |22\rangle \rightarrow |23\rangle$ with a three-photon resonance ($\delta_3 \approx 0$) at a fundamental wavelength of 4 317.32 nm and THG signal wavelength of

1 439.11 nm. Up-converting the THG signal with 532 nm pump radiation results in a SFM wavelength of 388.41 nm.

In contrast to HCl, the pressure of maximum signal is predicted at 15 mbar CO_2, without foreign gas. The absolute value of the nonlinear susceptibility at that resonance and pressure is with 30 000 pm^2/V^2 more than two orders of magnitude larger than the nonlinear susceptibility we calculated for HCl. Comparing the parameters for the nonlinear susceptibility for this excitation pathway with the parameters of HCl (see Tab. 3.1), the detunings are smaller with $\delta_1 = 12\,cm^{-1}$ and $\delta_2 = 1\,cm^{-1}$. Also, the $\Delta\nu = 1$ transition dipole moments are almost an order of magnitude larger ($\mu_{10} = 0.8 \times 10^{-30}$ C m, $\mu_{21} = 1.1 \times 10^{-30}$ C m, and $\mu_{32} = 1.3 \times 10^{-30}$ C m), while the overtone transition dipole moment is comparable with $\mu_{30} = 0.0018 \times 10^{-30}$ C m.

With these results, we turn to the experimental setup. A 150 mm focal length, CaF_2 lens with anti-reflection coating at 2-5 µm (LA5012-E, Thorlabs) focuses the fundamental beam of the modified laser setup into the center of the 18 cm long gas cell. There, it has a beam waist ($1/e^2$ radius) of 280 µm and a confocal parameter of 7 cm. In this chapter, the test gas are CO_2 gas samples (provided by Westfalen) with a purity of 99.995 %, for which we calibrated the pressure sensor in the gas cell with the method described in Sec. 3.3.4.

The detection setup is similar to the HCl up-conversion setup shown in Fig. 4.1 in Sec. 4.2, however, with suitable dichroic mirrors and filters for the fundamental radiation at 4 260 nm, the THG signal at 1 433 nm, and the SFM signal at 390 nm. The dichroic mirror DM between gas cell and APD (IAG-200-S6, Lasercomponents) is a CaF_2 mirror (Laseroptik) HR-coated for 1.4–1.8 µm and HT-coated for visible and mid-infrared wavelengths. In front of the APD is a longpass filter for 1 350 nm (LP1350, Thorlabs), and in front of the PMT (R14657, Hamamatsu) is a bandpass filter for 400 nm with 40 nm FWHM spectral width (FBH400-40, Thorlabs).

A.4 Experimental Results

Now, we turn our attention to the experimental results. We took small spectra around this three-photon resonance with the strongest THG signal by tuning the fundamental wavelength around 4 317 nm, while the gas cell was filled with 15 mbar CO_2. Figs. A.2 (a,b) show the THG and up-conversion SFM spectra, respectively. The number of generated THG photons is comparable to those obtained with HCl, although the fundamental pulse energy of 5 µJ was two orders of magnitude lower than in the up-conversion tests with HCl (see Ch. 4). This demonstrates that the larger nonlinear susceptibility is able to compensate the lower pulse energy, which enters cubically in the resulting pulse energy (see Eq. 1.1). However, the larger noise due to the laser system results in a smaller SNR of 7.

Contrary to our results with HCl, up-conversion of the THG signal to the visible at 388 nm does not improve the SNR, which is only 2. Also, the conversion efficiency is really low with only 1 % of the THG photons converted to visible photons. However, alignment and phase-matching of the SFM process was challenging, as both the THG and pump pulse energy fluctuated semi-independently, increasing the signal noise even more.

We also noted that the fundamental pulse energy increases to 30 µJ for the same

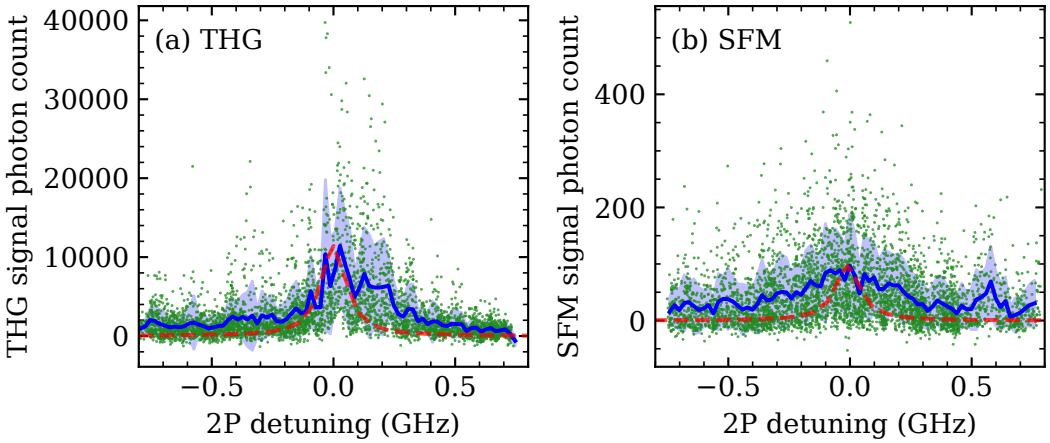

Figure A.2: (a) THG and (b) up-conversion SFM signal photon count vs. two-photon detuning from 4 317.33 nm with 15 mbar CO_2 in the gas cell. Green dots represent data points and the blue line and shaded area show the frequency binned data and standard deviation. The dashed red line represents the result of the numerical simulation. The fundamental pulse energy was 5 µJ, and, for up-conversion, the pump energy was 2.7 mJ.

pump pulse energy if we disable the Nd:YAG's seeder laser. We attribute this increase in pulse energy to the temporal spikes of the unseeded pulses in combination with the amplification threshold as these spikes cause overproportional amplification. Fig. A.3 (a) shows a THG spectrum around the three-photon resonance at 4 317 nm, while the gas cell was filled with 15 mbar CO_2. Most notably, the measured linewidth is many times larger than the simulated one (dashed red line), due to an increased fundamental pulse bandwidth. The dashed-dotted orange line shows a convolution of the simulation result with a Gaussian shaped fundamental bandwidth of 30 Ghz (FWHM), which conforms well to the measurement data. As the power amplifier amplifies a pulse with the same temporal profile, the pulse duration decreases and the bandwidth increases by a factor of $\sqrt{2}$. Consequently, the Nd:YAG bandwidth is 20 GHz, as expected from Ref. [27].

Also, the maximum of the wavelength binned signal is more than two orders or magnitude larger than in Fig. A.2 (a). At one hand, the THG pulse energy depends cubically on the fundamental pulse energy, which is almost an order of magnitude larger for an unseeded Nd:YAG laser. On the other hand, the convolution of the large laser bandwidth with the small resonance linewidth decreases the generated pulse energy by several orders of magnitude. In total, we expected less THG signal, not more. We attribute this discrepancy to the spikes in the temporal pulse shape, which generate an exponentially larger THG signal due to the cubic dependence.

These broadband pulses not only increase the generated THG signal, but also decreases the spectral resolution, such that they generate a measurable signal for detunings of a few GHz. This facilitates initial alignment of the detector setup, which requires both a suitable fundamental frequency to generate a measurable signal and a detector alignment to detect this signal. The broadband pulses ease the necessary frequency precision for the fundamental pulses to a few GHz, which is well in range of the wavemeters used, allowing mechanical alignment.

Finally, we used this increased THG signal to record a pressure dependence while

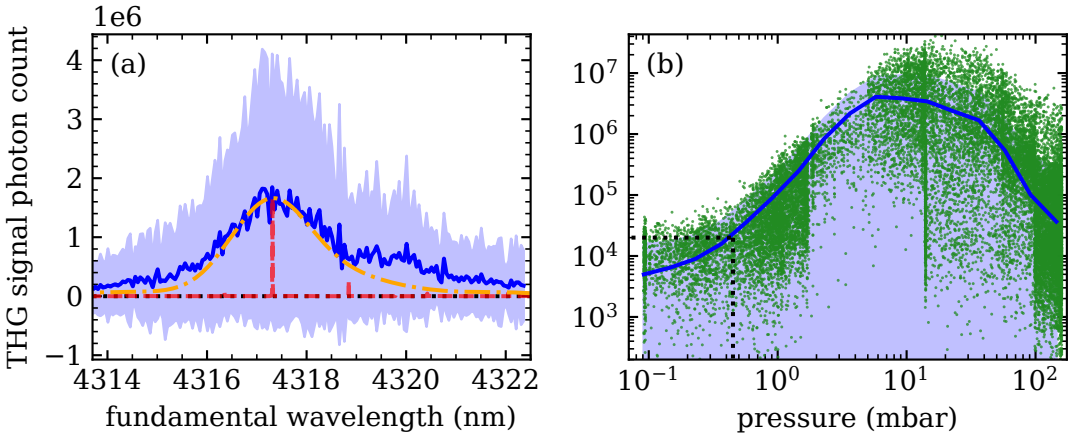

Figure A.3: THG signal photon count vs. (a) fundamental wavelength and (b) CO_2 pressure for a fundamental wavelength of 4 317.33 nm. Green dots represent data points, the blue line and shaded area the mean value and standard deviation. The dashed red line represents the numerical simulation, and the dashed-dotted orange line represents the numerical simulation convoluted with a 30 GHz (FWHM) Gaussian line form. Both lines are normalized to the maximum of the mean value. In (b), the dotted black lines indicate the detection limit, defined by the standard deviation envelope of the background noise. For both measurements, the Nd:YAG's injection seeder was disabled and the fundamental pulse energy was 30 µJ. Note that the photon count axis of (a) is in million photons. Note the logarithmic scales for both axes of the pressure dependence.

the fundamental wavelength is tuned to the three-photon resonance at 4 317.33 nm. Fig. A.3 (b) shows this pressure dependence. Pauses in the pressure scan, for changing neutral density filters in front of the PMT, cause the accumulation of data points on the pressure axis. The large distribution of data points across the photon count axis and the large standard deviation show the large fluctuations of the fundamental pulse energy. At 0.45 mbar, the mean signal is larger than the noise, defined as the standard deviation envelope of the mean background signal. For larger pressures, the THG signal increases, initially quadratically, reaches then its maximum at 15 mbar, as expected, and decreases again, down to barely negligible signal. Contrary to HCl, CO_2 has more dense single-photon transitions (a few GHz apart), several of which are close to the three-photon resonance, which absorb the fundamental radiation with increasing pressure.

A.5 Conclusion

We successfully built an OPO with an output power of up to 100 mW in the spectral range of 3 900 to 4 500 nm. This mid-infrared radiation was used to seed our modified OPA chain, which produced mid-infrared pulses with a pulse energy of up to 10 µJ. However, the primary factor limiting the performance was the high absorption of the amplifier material LNB, which we measured to be 80 % in a 3 cm crystal at a wavelength of 4 317 nm. This absorption not only reduced efficiency but also introduced a pump threshold, causing small fluctuations in the pump energy to result in large variations in the mid-infrared pulse energy.

Despite these challenges, the generated pulse energy and its fluctuations were sufficient to detect both the THG signal from CO_2 and its up-converted counterpart with SNRs of 7 and 2. With broadband fundamental pulses, we reached a detection limit for THG of 0.45 mbar. However, the energy of the system was insufficient to conduct systematic experiments. Consequently, we decided to revert back to use HCl as a test gas for further investigations.

We are currently developing a nanosecond OPO system, aiming to achieve higher pulse energies, which will allow us to revisit the study of THG in CO_2. The ns OPO shall generate pulses with an energy in the mJ range, at a wavelength of 1 439 nm, and with a pulse duration of several nanoseconds. At these shorter wavelengths, it should be possible to generate pulses with a higher pulse energy. We want to use these pulses to seed the power amplifier, thus we circumvent LNB's large absorption in the first stage while using a strong seed pulse in the power amplifier.

Appendix B

Laboratory Experiment Control Protocol Software

Initially, the measurement setup was controlled by Labview (NI) programs, but they proved to be rigid and challenging to adapt to changing requirements. To improve flexibility, the system was gradually transitioned to Python. This transition began with the author's development of a custom transmission control protocol (TCP)-based communication suite, which laid the groundwork for further advancements.

Building upon this foundation, the author, with significant feedback from the research community, defined the Laboratory Experiment Control Protocol (LECO) and implemented it in Python as PyLECO [52]. The following sections will present the core architecture and key features of LECO and its Python implementation.

B.1 Design Goals and Architecture of LECO

Before starting the definition process, we looked for existing solutions for a measurement framework offering modularity, flexibility, and ease of use. Some frameworks did not offer the modularity and flexibility we desired. PyMeasure offers at one hand instrument drivers and on the other hand a single-script measurement software, which ties up the whole experiment in a single process [53]. PyMoDAQ (Python Modular Data Acquisition [54]) is also a single process GUI based experiment control framework. Another framework (yaq [55]) requires the setup of instrument driver daemons contrary to our ease of use requirement. There are also large and feature rich frameworks, developed for large experimental facilities like particle accelerators. In theory, these frameworks (Tango, Sardana, Bluesky, etc.) could be applied to small experimental setups as well. However, their setup is too difficult for an average researcher running their own experiment.

Therefore, we defined the following goals for LECO:

1. Connect different solutions: instrument drivers from different libraries, a GUI from another library, and data acquisition from yet another library. They all might be written in different programming languages.

2. Enable small to medium sized experiments with approximately 50 participating software components, for example a few dozen instruments, a few GUI elements, a few control components, and a few data acquisition components.

3. Flexibility and modularity like *LEGO* building bricks in order to adapt to the changes of the experimental setup.

4. A simple, but powerful communication by communicating with user defined names, like sending emails.

5. Fast, but reliable communication, without dropped packages and a failing components should neither break the experimental setup nor corrupt already acquired data.

6. A low entry threshold and flat learning curve, in order get up and running in a matter of moments.

These goals led to the definition of LECO: The communication happens via messages (using ZeroMQ [56]) between participants (called *components*). ZeroMQ is a TCP based communication framework and offers therefore communication between different threads, processes, and physical devices independent of the programming language. It is more reliable and easier to use than raw TCP sockets.

Typically, at one hand a user wants to configure some instrument or read some instrument value, and on the other hand he expects to be informed about value changes or unexpected events. Therefore, there are two different communication protocols in LECO:

1. The control protocol allows to exchange messages between any two components in a LECO network, which is useful for controlling devices.

2. The data protocol is a broadcasting protocol to send information to all those, who have subscribed to receive it. It takes advantage of ZeroMQ's *PUB-SUB* pattern, which manages the subscribers in the background. This allows to implement event notifications like value changes, regular measurement data, or log entries.

Each message consists of a header and a content. The message header contains the name of the message's sender and, in the case of the control protocol, of the receiver of the message. A time-ordered, universally unique ID (UUIDv7) allows to identify a conversation (a request and the corresponding response) and an additional message id identifies a message in that conversation.

LECO defines the configuration of the sockets and format of the message header, which forms the transport layer. The content of the message, however, can be any bytes string, offering full flexibility to the user. Ref. [57] suggests this separation between transport layer and the content. We suggest JSON-RPC as the format of the content. As a remote procedure call (RPC) protocol, it defines the message format for calling the procedure of a remote program and for the response with the result or error. It uses JSON (JavaScript Object Notation) to encode the message, which makes the messages human readable and easy to debug. Compared to a binary encoding, the messages are typically small, as they mostly contain just the method name or a number as the return value. In case of larger objects, like oscilloscope traces or camera images, LECO offers the option to add these as additional binary payload. Alternatively any message encoding can be used with LECO.

The sender and receiver name in the header allow a server, called *coordinator*, to route the messages from the sender to the receiver. Several control protocol coordinators may connect to each other creating a large network over one or more computers. Each coordinator establishes a namespace with a unique name, typically the name of the host computer. Similarly, each component connected to a single coordinator has a name unique in that namespace, otherwise the coordinator

won't allow the connection. Therefore, the combination of namespace name and component name is unique in the whole network and allows to route a message to the intended recipient.

B.2 Python package PyLECO

Every protocol needs an implementation in code. We designed PyLECO as a library, written in Python, offering tools to communicate according to LECO. It is available on the Python Package Index (PyPI) and conda-forge, such that a simple command is sufficient to install it. Calling another script starts the control protocol or data protocol coordinator in order to establish the network infrastructure.

Controlling measurement devices is a common task for a measurement software. The PyLECO Actor encapsulates a measurement device driver (e.g. one offered by PyMeasure), such that any other participant may act on that measurement device via LECO communication. The Actor is single-threaded and handles one incoming message after the other, which prevents problems due to concurrent device access by different program parts.

Starting the Actors for each device in its own window clutters the user interface. Therefore, PyLECO's starter is able to start python scripts, for example containing an Actor, in individual threads. Obviously, the starter is also a LECO component, which allows to start, stop, or restart an Actor or any type of script remotely. The starter is also able to restart a script if it has stopped unexpectedly.

The last in this row of self-contained programs is the data logger, which logs and plots data published by different sources. This allows to collect data from measurement devices, view it for alignment or measurement control, and store it for data analysis and data publication.

PyLECO further offers utilities to send and receive messages via LECO in order to integrate LECO communication capabilities into a program for a measurement setup. Among these are the directors, which facilitate controlling a remote instrument, a coordinator, or the starter.

All these parts together allow to control measurement devices, acquire data, and perform scientific measurements with a measurement software distributed over several threads, processes, and computers.

Appendix C

Automation of Optical Parametric Amplifier

The efficient generation of mid-infrared light using OPOs and OPAs relies on precise phase-matching conditions. These conditions depend critically on the frequencies involved, which shift during wavelength scans, such as those performed for spectral measurements. In our experiments, we observed a significant drop in the output pulse energy from the power amplifier while tuning the mid-infrared frequency by several tens of GHz.

It is possible to regularly adjust the phase-matching angle during a frequency scan. However, besides being tedious, the output pulse energy varies between adjustments. To address this challenge, we implemented an automated system to dynamically adjust the phase-matching angle, ensuring optimal energy output throughout the wavelength scan.

In this chapter, we show the hardware setup, determine the power amplifier's acceptance bandwidth, describe the method, and present the results.

C.1 Setup and Acceptance Bandwidth

The experimental setup is the laser system as described in the Secs. 2.2 to 2.5. The two crystals are mounted on prism mounts (KM100PM/M, Thorlabs), with stepper motors (ZST206 and ZST213, Thorlabs) replacing the adjustment screws on the phase-matching axis. A single stepper motor card (TMCM-6110, Trinamic) controls the motors. The measurement software controls both the fiber laser's wavelength tuning and phase-matching angle at the same time. We measure the generated mid-infrared pulse energy with an energy meter (PE10-C, Ophir).

We determined the power amplifier's acceptance bandwidth by scanning the OPO pump wavelength and measuring the resulting mid-infrared pulse energy after having optimized the phase-matching angle for the center wavelength of the tuning range. The orange dots in Fig. C.1 show the mid-infrared pulse energy vs. the frequency detuning while the phase-matching angle is constant. At both ends of the spectrum, the output pulse energy drops to less than 50 % of the maximum pulse energy. The corresponding acceptance bandwidth is 160 GHz (FWHM).

C.2 Automated Phase-Matching Angle Adjustments

Although the motorized system allows for precise repositioning of the same phase-matching angles, we observed that the optimal phase-matching angle varies not only from day to day but even throughout a single day. Calculations using SNLO software indicate that a temperature fluctuation of just 4 K shifts the required phase-matching angle by 1.7 mrad, which is significantly larger than the acceptance angle (FWHM) of 0.19 mrad [58]. This means that even slight variations in crystal temperature —

especially since the crystals lack temperature control — can alter the phase-matching angle by a substantial portion of the acceptance angle.

However, the relative difference between phase-matching angles for two mid-infrared wavelengths remains unaffected by the small temperature variations common in the laboratory. Thus, once the phase-matching angle is optimized for a specific wavelength at a given crystal temperature, it becomes possible to accurately calculate and adjust the angle for other wavelengths. Through measurements of the crystals' rotation for different wavelengths, we determined that the crystals require a rotation of approximately 0.1 mrad per nanometer change in wavelength. This adjustment accounts for refraction at the crystals' entry surface. With this calibration, our system automatically adjusts the phase-matching angle during mid-infrared wavelength tuning.

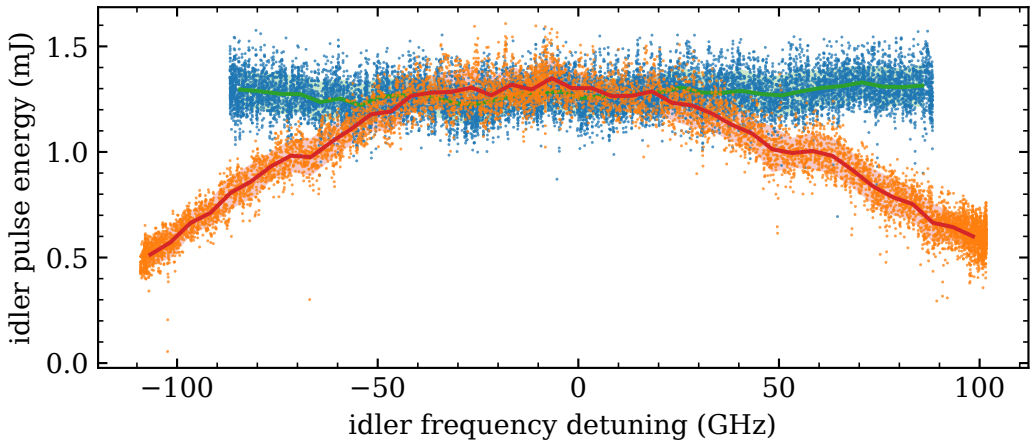

Figure C.1: Power amplifier idler pulse energy vs. frequency detuning around a center wavelength of 3495.7 nm. Blue dots represent the data with automated phase-matching angle adjustments, while the green line and shaded area represents the mean value and standard deviation. The orange dots and red line represent the data for a scan with fixed phase-matching angle.

The blue dots in Fig. C.1 represent the mid-infrared idler pulse energy at different idler wavelengths, with the stepper motors continuously adjusting the phase-matching angle for the corresponding frequencies. As a result, the mid-infrared pulse energy remains nearly constant across the entire scan range.

In conclusion, this automated phase-matching method maintains a stable mid-infrared pulse energy, which is crucial for processes like resonantly enhanced THG and SFM, where output depends cubically or quadratically on the fundamental pulse energy. For further details regarding the implementation refer to Ref. [59].

Bibliography

[1] W. Demtröder. *Laserspektroskopie 2: Experimentelle Techniken* 6. neu bearbeitete und aktualisierte Auflage (Springer Berlin Heidelberg Imprint Springer, Berlin, Heidelberg, 2013).

[2] J. Kiefer and P. Ewart. *Laser diagnostics and minor species detection in combustion using resonant four-wave mixing.* Progress in Energy and Combustion Science **37,** 525 (2011).

[3] M. R. Leahy-Hoppa *et al. Ultrafast Laser-Based Spectroscopy and Sensing: Applications in LIBS, CARS, and THz Spectroscopy.* Sensors **10,** 4342 (2010).

[4] R. L. Farrow and D. J. Rakestraw. *Detection of Trace Molecular Species Using Degenerate Four-Wave Mixing.* Science **257,** 1894 (1992).

[5] S. A. Druet and J.-P. E. Taran. *CARS spectroscopy.* Progress in Quantum Electronics **7,** 1 (1981).

[6] S. Roy, J. R. Gord, and A. K. Patnaik. *Recent advances in coherent anti-Stokes Raman scattering spectroscopy: Fundamental developments and applications in reacting flows.* Progress in Energy and Combustion Science **36,** 280 (2010).

[7] A. J. Traverso *et al. Two-Photon Infrared Resonance Can Enhance Coherent Raman Scattering.* Physical Review Letters **120,** 063602 (2018).

[8] J. F. Kinder. *Molecule Detection by Resonantly Enhanced Third Harmonic Generation of Mid-Infrared Laser Pulses.* PhD thesis (TU Darmstadt, 2021).

[9] J. A. Armstrong, N. Bloembergen, J. Ducuing, and P. S. Pershan. *Interactions between Light Waves in a Nonlinear Dielectric.* Physical Review **127,** 1918 (1962).

[10] J. Warner. *Parametric up-conversion from the infra-red.* Opto-electronics **3,** 37 (1971).

[11] A. Barh, P. J. Rodrigo, L. Meng, C. Pedersen, and P. Tidemand-Lichtenberg. *Parametric upconversion imaging and its applications.* Advances in Optics and Photonics **11,** 952 (2019).

[12] M. A. Albota and F. N. C. Wong. *Efficient single-photon counting at 1.55 μm by means of frequency upconversion.* Optics Letters **29,** 1449 (2004).

[13] M. J. Pellin and J. T. Yardley. *Resonanceenhanced infrared fourwave mixing by infraredactive molecules.* Applied Physics Letters **29,** 304 (1976).

[14] V. S. Dolzhikov, Y. S. Dolzhikov, A. A. Makarov, V. G. Movshev, and E. A. Ryabov. *Two-photon resonance spectroscopy of vibrational transitions in molecules under four-wave frequency mixing conditions.* Soviet Journal of Quantum Electronics **16,** 580 (1986).

[15] R. W. Boyd. *Nonlinear Optics* 4th ed. (Academic Press, London, 2020).

[16] G. Bjorklund. *Effects of focusing on third-order nonlinear processes in isotropic media.* IEEE Journal of Quantum Electronics **11,** 287 (1975).

[17] J. F. Kinder, B. Moneke, O. Ernst, and T. Halfmann. *Optical parametric oscillator and amplifier providing tunable, narrowband nanosecond laser pulses in the mid-infrared with mJ pulse energy.* Applied Physics B **128,** 188 (2022).

[18] G. F. Adams and C. F. Chabalowski. *Quantum Chemical Study of the Potential Energy Curves and Electronic Transition Strengths in HCl, XeCl, and HCl + Xe.* The Journal of Physical Chemistry **98,** 5878 (1994).

[19] I. Gordon *et al. The HITRAN2016 molecular spectroscopic database.* Journal of Quantitative Spectroscopy and Radiative Transfer **203,** 3 (2017).

[20] X. Ren *et al. Hydrogen chloride emissions from combustion of raw and torrefied biomass.* Fuel **200,** 37 (2017).

[21] A. A. Stec, T. R. Hull, K. Lebek, J. A. Purser, and D. A. Purser. *The effect of temperature and ventilation condition on the toxic product yields from burning polymers.* Fire and Materials **32,** 49 (2008).

[22] J. L. Dunham. *The Energy Levels of a Rotating Vibrator.* Physical Review **41,** 721 (1932).

[23] K. P. Huber and G. Herzberg. *Molecular spectra and molecular structure* (Van Nostrand Reinhold, New York, 1979).

[24] S. Tilford, M. Ginter, and J. T. Vanderslice. *Electronic spectra and structure of the hydrogen halides.* Journal of Molecular Spectroscopy **33,** 505 (1970).

[25] T. Parekunnel, T. Hirao, R. J. Le Roy, and P. F. Bernath. *FTIR Emission Spectra and Molecular Constants for DCl.* Journal of Molecular Spectroscopy **195,** 185 (1999).

[26] V. Mitura. *Setup of a Pulsed Mid Infrared Laser System for Resonantly Enhanced Third Harmonic Generation in CO_2.* MSc thesis (TU Darmstadt, 2023).

[27] R. Diaz *et al. Experimental evidence of temporal and spatial incoherencies of Q-switched Nd:YAG nanosecond laser pulses.* Applied Physics B **121,** 439 (2015).

[28] S. Schaffrath. *Aufbau eines Vakuum-Raumfilters zur Frequenzkonversion nah-infraroter Strahlung in den sichtbaren Spektralbereich.* BSc thesis (TU Darmstadt, 2022).

[29] D. J. Armstrong, W. J. Alford, T. D. Raymond, A. V. Smith, and M. S. Bowers. *Parametric amplification and oscillation with walkoff-compensating crystals.* Journal of the Optical Society of America B **14,** 460 (1997).

[30] S. Lin, Y. Tanaka, S. Takeuchi, and T. Suzuki. *Improved dispersion equation for $MgO:LiNbO_3$ crystal in the infrared spectral range derived from sum and difference frequency mixing.* IEEE Journal of Quantum Electronics **32,** 124 (1996).

[31] B. Moneke, J. F. Kinder, O. Ernst, and T. Halfmann. *Detection of HCl molecules by resonantly enhanced sum-frequency mixing of mid- and near-infrared laser pulses.* Physical Review A **107,** 012803 (2023).

[32] J. Tennyson *et al. Recommended isolated-line profile for representing high-resolution spectroscopic transitions (IUPAC Technical Report).* Pure and Applied Chemistry **86,** 1931 (2014).

[33] J. Olivero and R. Longbothum. *Empirical fits to the Voigt line width: A brief review.* Journal of Quantitative Spectroscopy and Radiative Transfer **17,** 233 (1977).

[34] J. E. Chamberlain, F. D. Findlay, and H. A. Gebbie. *The Measurement of the Refractive Index Spectrum of HCl Gas in the Near Infrared Using a Michelson Interferometer.* Applied Optics **4,** 1382 (1965).

[35] R. Rollefson and A. H. Rollefson. *The Optical Dispersion of HCl in the Infrared.* Physical Review **48,** 779 (1935).

[36] B. Burger, J. F. Kinder, P. Christ, and N. Stewen. Simulation of Resonantly Enhanced Third Harmonic Generation in Molecular Gases [Software]. Version v0.2.0. 2024. doi:10.5281/zenodo.11261875.

[37] J. F. Kinder, F. Cipura, and T. Halfmann. *Detection of HCl molecules by resonantly enhanced third-harmonic generation, driven by midinfrared laser pulses.* Physical Review A **103,** 052808 (2021).

[38] J. S. Otto. *Aufbau und Charakterisierung eines optisch parametrischen Verstärkers für mittel-infrarote ns-Pulse.* MSc thesis (TU Darmstadt, 2018).

[39] O. Ernst. *Resonantly Enhanced Sum Frequency Mixing and Third Harmonic Generation in HCl.* MSc thesis (TU Darmstadt, 2022).

[40] K. Jousten. *On the gas species dependence of Pirani vacuum gauges.* Journal of Vacuum Science & Technology A: Vacuum, Surfaces, and Films **26,** 352 (2008).

[41] G. D. Boyd and D. A. Kleinman. *Parametric Interaction of Focused Gaussian Light Beams.* Journal of Applied Physics **39,** 3597 (1968).

[42] Y. Furukawa *et al. Investigation of bulk laser damage threshold of lithium niobate single crystals by* Q *-switched pulse laser.* Journal of Applied Physics **69,** 3372 (1991).

[43] U. Bäder *et al. Pulsed nanosecond optical parametric generator based on periodically poled lithium niobate.* Optics Communications **217,** 375 (2003).

[44] N. Muthreich. *Frequenzkonversion infraroter Strahlung in den nahen UV-Bereich.* BSc thesis (TU Darmstadt, 2023).

[45] M. Aresta and A. Dibenedetto. *The Carbon Dioxide Revolution: Challenges and Perspectives for a Global Society* (Springer International Publishing, Cham, 2021).

[46] J. F. Triana, D. Peláez, M. Hochlaf, and J. L. Sanz-Vicario. *Ultrafast CO_2 photodissociation in the energy region of the lowest Rydberg series.* Physical Chemistry Chemical Physics **24,** 14072 (2022).

[47] T. Shimanouchi. *Tables of molecular vibrational frequencies* (National Bureau of Standards, Washington, DC, 1972).

[48] L. Kaul. *Absorptionsspektroskopie von CO_2 mittels eines mittelinfraroten OPO-Lasersystems.* BSc thesis (TU Darmstadt, 2022).

[49] B. Burger. *Optical Parametric Oscillator.* Version 1.0.0 (Zenodo, 2022). doi:10.5281/zenodo.7408450.

[50] B. Moneke. *Setup of a Tunable, Narrowband, Continuous Wave Optical Parametric Oscillator at 606 nm.* MSc thesis (TU Darmstadt, 2020).

[51] K. Drühl. *Dispersion-induced generation of higher order transversal modes in singly-resonant optical parametric oscillators.* Optics Communications **145,** 5 (1998).

[52] B. Burger, B. Klebel-Knobloch, and C. Buchner. PyLECO [Software]. Version 0.3.1. PyMeasure, 2024. doi:10.5281/zenodo.10964073.

[53] Colin Jermain *et al.* PyMeasure [Software]. Version 0.13.1. PyMeasure, 2024. doi:10.5281/zenodo.595633.

[54] S. J. Weber. *PyMoDAQ: An open-source Python-based software for modular data acquisition.* Review of Scientific Instruments **92,** 045104 (2021).

[55] K. F. Sunden *et al. The yaq project: Standardized software enabling flexible instrumentation.* Review of Scientific Instruments **94,** 044707 (2023).

[56] *ZeroMQ.* https://zeromq.org/ (2024).

[57] J. Lauener and W. Sliwinski. *How to Design & Implement a Modern Communication Middleware Based on ZeroMQ.* Proceedings of the 16th Int. Conf. on Accelerator and Large Experimental Control Systems **ICALEPCS2017** (2018).

[58] A. V. Smith. SNLO nonlinear optics code [Software]. Version 79. Albuquerque, NM: AS-Photonics, 2023.

[59] F. Wanitschke. *Automatisierte Wellenlängendurchstimmung eines optisch parametrischen Verstärkers für die Spektroskopie.* BSc thesis (TU Darmstadt, 2022).

Publications and Contributions to Conferences

Publications in Peer-Reviewed Journals

- J. F. Kinder, B. Moneke, O. Ernst, and T. Halfmann.
  Optical parametric oscillator and amplifier providing tunable, narrowband nanosecond laser pulses in the mid-infrared with mJ pulse energy.
  Applied Physics B **128**, 188 (2022)

- B. Moneke, J. F. Kinder, O. Ernst, and T. Halfmann
  Detection of HCl molecules by resonantly enhanced sum-frequency mixing of mid- and near-infrared laser pulses.
  Physical Review A **107**, 012803 (2023)

Manuscripts in Preparation

- B. Burger and T. Halfmann.
  Frequency up-conversion of mid-infrared signals from resonantly enhanced nonlinear spectroscopy.

Talks at international conferences

- B. Burger.
  Driver library PyMeasure.
  Journées thématiques PyMoDAQ 2023 - Paris (France), October 2023

- B. Burger.
  PyLECO and its integration in PyMoDAQ.
  Journées thématiques PyMoDAQ 2024 - Lyon (France), October 2024

Supervisions and Contributions to Teaching

Master's Thesis

- Oskar Ernst, *Resonantly Enhanced Sum Frequency Mixing and Third Harmonic Generation in HCl*, 2022
- Viktor Mitura, *Setup of a Pulsed Mid Infrared Laser System for Resonantly Enhanced Third Harmonic Generation in CO_2*, 2023

Bachelor's Thesis

- Denise Schwarz, *Frequenzkonversion mittel-infraroter Strahlung in den sichtbaren Spektralbereich*, 2022
- Felix Wanitschke, *Automatisierte Wellenlängendurchstimmung eines optisch parametrischen Verstärkers für die Spektroskopie*, 2022
- Lisa Kaul, *Absorptionsspektroskopie von CO_2 mittels eines mittelinfraroten OPO-Lasersystems*, 2022
- Nils Muthreich, *Frequenzkonversion infraroter Strahlung in den nahen UV-Bereich*, 2023

Internships "Miniforschung"

- Felix Wanitschke, *Charakterisierung der zwei optischen parametrischen Verstärker am Aufbau zur nichtlinearen Spektroskopie*, 2021
- Elias Hamel, *Kalibrierung eines Drucksensors zur Absorptionsspektroskopie von CO_2 Molekülen*, 2022
- Abdelhamid Ettahri, *Vermessung und Kollimation eines mittel-infraroten Strahls*, 2024

Contributions to Teaching

- Head of basic lab course department *electricity* 2020-2023
- Labtours 2020-2024
- Supervision of exercise groups: mathematical preparation course 2024

Erklärungen gemäß Promotionsordnung

§8 Abs. 1 lit. c PromO
Ich versichere hiermit, dass die elektronische Version meiner Dissertation mit der schriftlichen Version übereinstimmt.

§8 Abs. 1 lit. d PromO
Ich versichere hiermit, dass zu einem vorherigen Zeitpunkt noch keine Promotion versucht wurde. In diesem Fall sind nähere Angaben über Zeitpunkt, Hochschule, Dissertationsthema und Ergebnis dieses Versuchs mitzuteilen.

§9 Abs. 1 PromO
Ich versichere hiermit, dass die vorliegende Dissertation selbstständig und nur unter Verwendung der angegebenen Quellen verfasst wurde.

§9 Abs. 2 PromO
Die Arbeit hat bisher noch nicht zu Prüfungszwecken gedient.

Darmstadt, 15. Oktober 2024

(Benedikt Burger)